Volume complexity for Janus AdS₃ geometries

Roberto Auzzi,[a,b] Stefano Baiguera,[c] Sara Bonansea,[c] Giuseppe Nardelli[a,d]
and Kristian Toccacelo[c]

[a]*Dipartimento di Matematica e Fisica, Università Cattolica del Sacro Cuore,*
Via Musei 41, 25121 Brescia, Italy

[b]*INFN Sezione di Perugia,*
Via A. Pascoli, 06123 Perugia, Italy

[c]*The Niels Bohr Institute, University of Copenhagen,*
Blegdamsvej 17, DK-2100 Copenhagen Ø, Denmark

[d]*Trento Institute for Fundamental Physics and Applications (TIFPA) — INFN,*
c/o Dipartimento di Fisica, Università di Trento,
Via Sommarive 14, I-38123 Povo (TN), Italy

E-mail: roberto.auzzi@unicatt.it, stefano.baiguera@nbi.ku.dk,
sara.bonansea@nbi.ku.dk, giuseppe.nardelli@unicatt.it,
btm438@alumni.ku.dk

Abstract: We investigate the complexity=volume proposal in the case of Janus AdS₃ geometries, both at zero and finite temperature. The leading contribution coming from the Janus interface is a logarithmic divergence, whose coefficient is a function of the dilaton excursion. In the presence of the defect, complexity is no longer topological and becomes temperature-dependent. We also study the time evolution of the extremal volume for the time-dependent Janus BTZ black hole. This background is not dual to an interface but to a pair of entangled CFTs with different values of the couplings. At late times, when the equilibrium is restored, the couplings of the CFTs do not influence the complexity rate. On the contrary, the complexity rate for the out-of-equilibrium system is always smaller compared to the pure BTZ black hole background.

Contents

1 Introduction

Since the discovery of the Bekenstein-Hawking formula for the entropy, there has been a greater understanding of the quantum information properties encoded by the geometry of spacetime via holography. One of the biggest achievements of this idea in the context of AdS/CFT was the Hubeny-Ryu-Takayanagi (HRT) formula [1, 2], which relates the

entanglement entropy for a subregion on the boundary to the area of a codimension-two extremal surface γ anchored to the boundary of the subsystem, that is,

$$S_A = \frac{A(\gamma)}{4G}\,. \tag{1.1}$$

This holographic proposal was justified from the perspective of the gravitational path integral [3] and later generalized to include quantum corrections [4]. These advancements led to the concept of generalized extremal surfaces, a prescription where the fine-grained entropy of a system is computed by extremizing the sum of the HRT entropy and a contribution which accounts for the quantum corrections due to matter fields. In particular, this conjecture was used to recover the Page curve for evaporating black holes [5–7].

The area of codimension-two extremal surfaces plays a central role in holography. It is then natural to wonder about the meaning of the volume of codimension-one objects, whose role is not yet well established in holography. The most promising proposal is, arguably, that of holographic complexity [8]. Other related possibilities include the concepts of quantum information metric and fidelity [9, 10].

Motivated by the desire of finding a dual description to the growth of the Einstein-Rosen Bridge (ERB) in black holes, Susskind and collaborators [8, 11, 12] introduced the notion of computational complexity in holography. By studying the time evolution of wormholes, e.g., an eternal Black Hole (BH) in asymptotically AdS spacetime, one can figure out that spacelike slices connecting the two asymptotic boundaries evolve for a much longer time compared to the thermalization time scale. Since these slices can be defined in a coordinate-invariant way by selecting the one with maximal volume at each value of time, it is expected that there exists a dual quantity on the field theory side. In [8] it was conjectured that the dual is computational complexity, which is heuristically defined as a measure of the minimal number of simple unitary operations relating a reference state with a chosen target state. For quantum mechanical systems, complexity can be defined geometrically as a Hamiltonian control problem, an approach pioneered by Nielsen et al. [13, 14]; in this approach, negative curvatures seem to be a desirable feature of complexity space [15–17]. While there has been some recent progress in extending Nielsen's method to free field theory [18–20], a precise definition of complexity in interacting CFTs is still lacking. Further developments in this direction can be found in, e.g., [21–23]. Other approaches have also gained attention in the community, see for instance [24–26].

Two proposals have made their way as holographic duals to computational complexity:

- the Complexity=Volume conjecture (CV), where the complexity is proportional to the volume of a maximal spacelike codimension-one surface Γ anchored at the boundary

$$\mathcal{C}_V \sim \frac{V(\Gamma)}{GL}\,, \tag{1.2}$$

where L is the AdS radius. This proposal has been tested in geometries with shock waves perturbations and reproduced phenomena expected from tensor networks and quantum circuits [11]; and

- the Complexity=Action conjecture (CA). Since the CV conjecture is not universal (it contains a specific dependence from a length scale like the AdS radius), it was later proposed that the complexity is holographically given by the gravitational action I computed in the Wheeler-De Witt (WDW) patch, i.e., the bulk domain of dependence of the ERB [27, 28]:

$$\mathcal{C}_A = \frac{I_{\text{WdW}}}{\pi}\,. \tag{1.3}$$

The late time behaviour of volume and action for asymptotically AdS black holes is found to be qualitatively the same, but they differ for intermediate times [29].

The previous proposals have natural generalisation to the case of mixed states. In the CV case, the proposal is to compute the volume of a maximal slice anchored to a boundary subregion and bounded by the corresponding HRT surface [10]: hence the name *subregion complexity*. To compute subregion CA, it was proposed [30] to evaluate the gravitational action on the intersection of the WDW patch and the entanglement wedge. Subregion complexity for an arbitrary interval in a BTZ black hole [31] background is an example where volume and action proposals behave differently [32, 33]. Further studies on subregion complexity include [34–39].

Defects, interfaces and boundaries are often present in interesting physical systems. Impurities are one of the main topics in condensed matter physics. From a field theory perspective, we can model these systems as a renormalization group (RG) flow where bulk and boundary degrees of freedom are coupled. Entanglement entropy also provides an important tool to characterize the properties of defects under RG flow. The entanglement entropy S of an interval with length l in a two-dimensional CFT centered around the defect has the following form [40]

$$S = \frac{c}{3} \log \frac{l}{\delta} + \log g\,, \tag{1.4}$$

where c is the central charge, δ the UV cutoff, and g the ground state degeneracy of the defect. The quantity g is monotonic under RG flow [41] and gives a measure of the number of degrees of freedom localised on the defect.

Holographic examples of geometries dual to defect CFTs include:

- the Randall-Sundrum model (RS) [42]. The simplest situation corresponds to a two-dimensional brane embedded in AdS$_3$, as considered in [43] for the study of entanglement entropy. The case of a conformal defect in d dimensions was recently investigated in the context of the island conjecture in relation to subregion complexity [44];

- the holographic dual of CFT with boundaries (BCFT) studied in [45–47]; and

- Janus geometries [48, 49]. While it was originally discovered as a non-supersymmetric dilatonic deformation of AdS$_5$ space [48], it was later found that a similar deformation can be implemented on AdS$_3 \times S^3 \times M_4$, where M_4 is a compact manifold [49]. Since these solutions can be embedded into type IIB supergravity, they have well-defined top-down holographic duals.

All these geometries are interesting laboratories to investigate quantum information aspects of the AdS/CFT duality. The Janus geometry was recently considered as a background to test the pseudo-entropy, a quantum information object which is conjectured to describe a Euclidean version of the entanglement entropy [50].

The physics of defects may provide us deeper insights on holographic complexity. While this was already studied previously for the three-dimensional RS model in [51] and for BCFT [52, 53], the purpose of this paper is to fill the gap for three-dimensional Janus geometries. Related studies focusing on fidelity can be found in [9, 54, 55]. These backgrounds represent an important playground to test the behavior of holographic complexity because they admit many deformations with well-defined holographic duals, including the finite temperature case or time-dependent perturbations.

In section 2 we review some basic facts about Janus geometries in three dimensions. In section 3 we compute the subregion volume complexity for a symmetric region with radius $l/2$ around the defect in Janus AdS$_3$. The pure state complexity can be extracted from the $l \to \infty$ limit of this result, where the length l plays the role of an IR regulator. In section 4 we extend the calculation at finite temperature, by computing the volume of the static BTZ Janus black hole at time $t = 0$. In section 5 we consider CV for the time-dependent Janus BTZ black hole. In this situation, the dual theory is not a defect CFT, but it corresponds to two entangled CFTs with different values of the dilaton field on each side of the Penrose diagram. We determine the time dependence of volume complexity for this situation. We summarize our results in section 6. Appendix A contains our conventions for Jacobi elliptic functions and elliptic integrals.

2 Janus geometry

In this section we introduce some of the faces that the Janus geometry can assume. The Janus solution is a dilatonic domain-wall deformation of spacetime whose dual description is an interface CFT (ICFT). We focus on the three-dimensional space, starting with the Janus deformation of empty AdS$_3$ space described in section 2.1. Complexity requires the introduction of UV regulators; these are naturally determined from the Fefferman-Graham (FG) expansion of the metric, which is considered in section 2.2. In section 2.3 we present the conformal structure of the Janus AdS background, while in section 2.4 we extend the static Janus deformation to the case of the BTZ black hole solution.

2.1 Janus AdS$_3$

The Janus AdS$_3$ solution [49] can be obtained from type IIB supergravity on AdS$_3 \times S^3 \times M_4$, where M_4 can be chosen either as T^4 or $K3$. Upon dimensional reduction, the following action is obtained

$$I = \frac{1}{16\pi G} \int d^3x \sqrt{-g} \left(R - \partial^a \phi \partial_a \phi + \frac{2}{L^2} \right), \tag{2.1}$$

where ϕ is the dilaton and L the AdS$_3$ radius.

We will use the metric ansatz

$$ds^2 = L^2 (f(y) ds^2_{\text{AdS}_2} + dy^2), \tag{2.2}$$

where $ds^2_{\text{AdS}_2}$ denotes the generic AdS$_2$ metric in arbitrary coordinates. Unless otherwise specified, we will describe the AdS slices using Poincaré coordinates, that is,

$$ds^2 = L^2 \left(f(y) \frac{dz^2 - dt^2}{z^2} + dy^2 \right) . \tag{2.3}$$

Solving the equation of motion, the following solution is obtained

$$f(y) = \frac{1}{2} \left(1 + \sqrt{1 - 2\gamma^2} \cosh(2y) \right) ,$$
$$\phi(y) = \phi_0 + \frac{1}{\sqrt{2}} \log \left(\frac{1 + \sqrt{1 - 2\gamma^2} + \sqrt{2}\gamma \tanh y}{1 + \sqrt{1 - 2\gamma^2} - \sqrt{2}\gamma \tanh y} \right) , \tag{2.4}$$

where the coordinate y is ranged in $(-\infty, +\infty)$. In correspondence of the extrema $y = \pm\infty$ we have two boundaries, where the two sides of the interface field theory live. The parameter ϕ_0 is set by the value of the dilaton at $y = 0$. The constant $\gamma \in [0, \sqrt{2}/2]$ parameterizes the excursion of the dilaton between the two sides. For $\gamma = 0$ the dilaton is constant and the solution is just empty AdS.

The dual interpretation of this metric is a two-dimensional CFT deformed by a marginal operator $O(x)$ with couplings $J_\pm \int d^2x \, O(x)$ on each boundary, where

$$J_\pm = \lim_{y \to \pm\infty} \phi(y) . \tag{2.5}$$

The bulk coordinate y connects two theories with different coupling constants living at $y = \pm\infty$. For $\gamma = \sqrt{2}/2$, the dilaton is linear, i.e., $\phi = \phi_0 + \sqrt{2}y$ and f is constant. In this limit the dilaton is divergent at the boundary, and the bulk theory is infinitely strongly coupled. Since the Janus deformation is associated with an exactly marginal operator, it does not change the central charge of the CFT.

For later purposes, it is useful to perform the change of variable $\mu(y)$ such that

$$d\mu = \frac{dy}{\sqrt{f(y)}} . \tag{2.6}$$

In the new set of coordinates the metric is

$$ds^2_3 = L^2 f(y(\mu)) \cos^2 \mu \, ds^2_{\text{AdS}_3} , \qquad ds^2_{\text{AdS}_3} = \frac{1}{\cos^2 \mu} \left(d\mu^2 + ds^2_{\text{AdS}_2} \right) . \tag{2.7}$$

The function $f(\mu) = f(y(\mu))$ and the dilaton can be expressed [56] in terms of Jacobi elliptic functions (see appendix A for our conventions)

$$f(\mu) = \frac{\alpha_+^2}{\text{sn}^2 \left(\alpha_+(\mu + \mu_0), m \right)} ,$$
$$\phi(\mu) = \phi_0 + \sqrt{2} \log \left[\text{dn} \left(\alpha_+(\mu + \mu_0), m \right) - \sqrt{m} \, \text{cn} \left(\alpha_+(\mu + \mu_0), m \right) \right] , \tag{2.8}$$

where

$$\alpha_\pm^2 = \frac{1}{2} \left(1 \pm \sqrt{1 - 2\gamma^2} \right) , \qquad m = \left(\frac{\alpha_-}{\alpha_+} \right)^2 , \qquad \mu_0 = \frac{\mathbb{K}(m)}{\alpha_+} . \tag{2.9}$$

The range of the new coordinate μ is $[-\mu_0, \mu_0]$. Note that when $\gamma = 0$ we get $\mu_0 = \pi/2$ and we recover the AdS case with constant dilaton ϕ_0 and $f(\mu) = 1/\cos^2 \mu$.
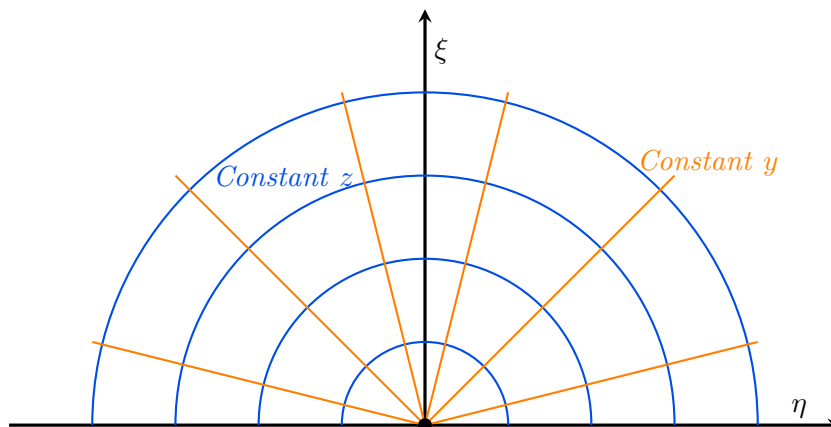
Figure 1. Foliation of the AdS$_3$ geometry into AdS$_2$ slices, where the lines at constant y and z coordinates are depicted. The black dot in the origin is the location of the Janus interface.

2.2 UV regulator and Fefferman-Graham expansion

A standard procedure for regularizing AdS-sliced metrics is to introduce a constant cut-off along the radial direction in a Fefferman-Graham (FG) expansion of the metric (see, e.g., [57] and [58]). Let's start by considering the AdS$_2$-sliced metric for the pure AdS$_3$ geometry,

$$ds^2_{\text{pure}} = L^2 \left(dy^2 + \cosh^2 y \, \frac{dz^2 - dt^2}{z^2} \right) , \tag{2.10}$$

that is, the Janus geometry with $\gamma = 0$. The boundary parameterization of AdS$_3$ in the coordinates (2.10) is more complicated compared to the one in Poincaré coordinates. In fact, the two $(1+1)-$dimensional boundaries at $y \to \pm\infty$ in (2.10) sit on the same boundary when represented in Poincaré coordinates. Let us first relate the metric (2.10) to the same metric in Poincaré coordinates

$$ds^2_{\text{pure}} = \frac{L^2}{\xi^2} \left(d\xi^2 + d\eta^2 - dt^2 \right) , \tag{2.11}$$

by implementing the change of variables (see figure 1)

$$\eta = z \tanh y , \qquad \xi = \frac{z}{\cosh y} . \tag{2.12}$$

Coming back to the Janus geometry in eq. (2.2), we can see that in the boundary regions $y \to \pm\infty$ the metric can be approximated by

$$ds^2_{\pm\infty} = L^2 \left(dy^2 + \frac{\sqrt{1 - 2\gamma^2}}{4} e^{\pm 2y} \frac{dz^2 - dt^2}{z^2} \right) . \tag{2.13}$$

Equation (2.13) simplifies by shifting the y coordinate as follows

$$\tilde{y} = y \pm \frac{1}{2} \log \sqrt{1 - 2\gamma^2}, \quad ds^2_{\pm\infty} = L^2 \left(d\tilde{y}^2 + \frac{1}{4} e^{\pm 2\tilde{y}} \frac{dz^2 - dt^2}{z^2} \right) . \tag{2.14}$$

We can then introduce the FG coordinates (ξ, η):

- when $\tilde{y} \to \infty$, $\xi \to 0$, and $\eta > 0$

$$e^{-2\tilde{y}} = \frac{1}{4}\frac{\xi^2}{\eta^2}, \qquad z = \eta \left(1 + \frac{1}{2}\frac{\xi^2}{\eta^2}\right), \tag{2.15}$$

- when $\tilde{y} \to -\infty$, $\xi \to 0$, and $\eta < 0$

$$e^{2\tilde{y}} = \frac{1}{4}\frac{\xi^2}{\eta^2}, \qquad z = |\eta| \left(1 + \frac{1}{2}\frac{\xi^2}{\eta^2}\right). \tag{2.16}$$

Therefore, the metric in eq. (2.13) becomes

$$ds^2_{\pm\infty} = \frac{L^2}{\xi^2}\left(d\xi^2 + d\eta^2 - dt^2 + \mathcal{O}(\xi)\right). \tag{2.17}$$

This is valid when we are far from the interface located at $(\eta, \xi) = 0$. In fact, close to the origin the coordinate transformation is singular and a different cutoff should be introduced. More precisely, the regime where the FG expansion is valid is $\xi \ll \eta$, which implies that at the lowest order $|\eta| \simeq z$, see eqs. (2.15) and (2.16). We will discuss how to regularize divergences in the region close to the interface in section 3.2.

2.3 Conformal diagram of the Janus geometry

In order to understand the geometrical properties of Janus, it is useful to consider the conformal diagram. It can be obtained by identifying an appropriate conformal factor multiplying a known metric. Starting from eq. (2.7), and choosing the AdS$_2$ slices in Poincaré coordinates, we obtain

$$ds^2_3 = \frac{L^2}{z^2} f(\mu) \left(z^2 d\mu^2 + dz^2 - dt^2\right). \tag{2.18}$$

This metric is conformal to a portion of the Minkowski spacetime where the spatial part is written in polar coordinates with angle $-\mu_0 \leq \mu \leq \mu_0$ and radius $z > 0$. This conformal diagram is depicted in figure 2. Since $\mu_0 \geq \pi/2$, the junction between the half-boundaries meets at a joint[1] W with an obtuse angle.

We can also consider the case where global coordinates are taken on AdS$_2$ the slicing, which gives the metric

$$ds^2 = \frac{L^2}{\cos^2 \lambda}\left(-dt^2 + \cos^2 \lambda\, d\mu^2 + d\lambda^2\right), \tag{2.19}$$

and the associated conformal diagram is given in figure 3. The boundary consists of two parts, defined by $\mu = \pm\mu_0$, which are given by two halves of S^1 joined through the north and south poles.

---

[1]While this joint seems singular, it can be shown that it is only an artifact of the coordinate system.
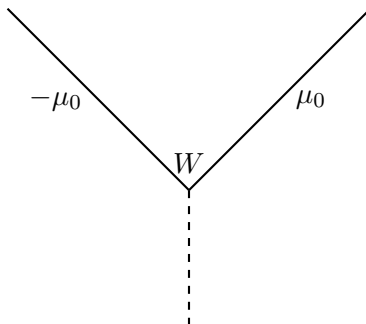
Figure 2. Conformal diagram taken from [48] for the Janus AdS$_3$ geometry with Poincaré coordinates on the AdS$_2$ slices. The polar angle corresponds to the coordinate $\mu \in [-\mu_0, \mu_0]$ and the radial coordinate is $z \in [0, \infty]$. The joint W corresponds to the place where the two parts with the topology of half $\mathbb{R}^2$ meet. It can be seen as a domain wall on the boundary.
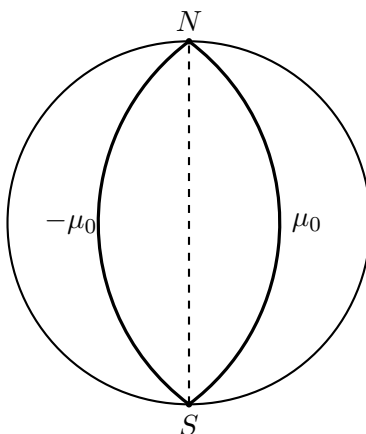
Figure 3. Conformal diagram for the Janus AdS$_3$ geometry with global coordinates on the AdS$_2$ slices.

2.4   Static Janus BTZ black hole

The static Janus BTZ background [59, 60] is dual to the Janus interface conformal field theory at finite temperature. The Kruskal extension of this solution is dual to two copies of the Janus interface CFT in the thermofield double state. This solution has a timelike Killing vector, hence the name static. It can be obtained as follows.

Starting from the Janus AdS metric

$$ds^2 = L^2 \left(dy^2 + f(y)\, ds^2_{\text{AdS}_2} \right) = L^2 f(\mu) \left(d\mu^2 + ds^2_{\text{AdS}_2} \right), \qquad (2.20)$$

one can replace Poincaré AdS$_2$ with Rindler AdS

$$ds^2_{\text{AdS}_2} \rightarrow ds^2_{\text{Rindler}} = -\frac{(w^2 - 1)\, r_h^2}{L^4} dt^2 + \frac{dw^2}{w^2 - 1}. \qquad (2.21)$$

For $\gamma = 0$, the interfaces on each boundary disappear and the solution coincides with the
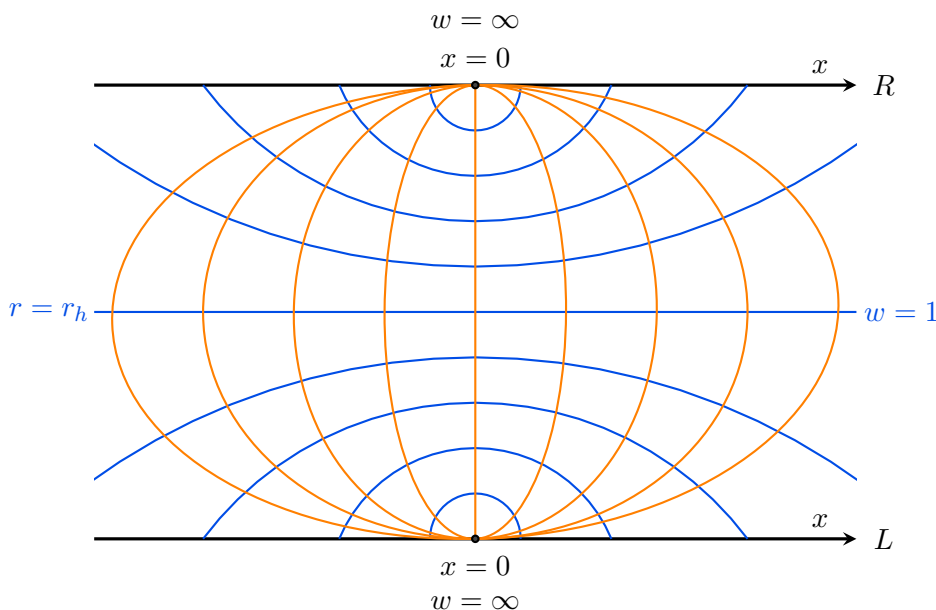
Figure 4. Picture representing an AdS slice of the BTZ black hole at constant time. The lines at constant w are depicted in blue, while the curves at constant μ in orange. The coordinate x runs along the left (L) and right (R) disconnected boundaries. The coordinate r covers the region outside the horizon and runs on the vertical axis: starting from the middle line located at $r = r_h$, it increases towards the L and R boundaries.

BTZ black hole [31]. This can be seen from the change of coordinates (see figure 4)

$$\frac{r_h}{r} = \frac{\cos\mu}{\sqrt{w^2 - \sin^2\mu}}, \qquad \sinh\frac{r_h x}{L^2} = \frac{\sin\mu}{\sqrt{w^2 - \sin^2\mu}}, \tag{2.22}$$

which bring the metric in eqs. (2.20) and (2.21) to the familiar form of the BTZ black hole with vanishing angular momentum

$$ds_{\text{BTZ}}^2 = -\frac{r^2 - r_h^2}{L^2} dt^2 + \frac{L^2 dr^2}{r^2 - r_h^2} + \frac{r^2}{L^2} dx^2. \tag{2.23}$$

The horizon is at $r = r_h$ and $r = 0$ corresponds to an orbifold singularity. This solution is invariant under time t and spatial x translations. When the deformation parameter γ is non vanishing, translational invariance in x is broken, while the time translation symmetry in t remains unbroken. When $\gamma = 0$, due to translational invariance in x, we can compactify $x \sim x + 2\pi$. For general γ, this identification is no longer consistent with the symmetries of the problem.

For generic γ the asymptotic behaviour of the solution can be mapped to the asymptotics of the BTZ as follows

$$\frac{r}{r_h} \simeq \sqrt{(w^2 - 1)f(y) + 1}, \qquad \sinh\frac{r_h x}{L^2} \simeq \text{sign}(x)\sqrt{\frac{f(y) - 1}{(w^2 - 1)f(y) + 1}}. \tag{2.24}$$

At generic γ, the solution has a Killing vector ∂_t, which corresponds to time translations. When considering the Kruskal extension of the solution, this Killing vector corresponds to

the following time translations on the left and right boundaries

$$t_L \to t_L \pm \Delta t, \qquad t_R \to t_R \mp \Delta t, \tag{2.25}$$

The field theory dual involves the left and the right interface CFTs in the thermofield (TFD) double state

$$|\psi(t_L, t_R)\rangle = e^{-i(t_L\, H \otimes \mathbf{1} + t_R\, \mathbf{1} \otimes H)}|\psi(0,0)\rangle, \qquad |\psi(0,0)\rangle = \frac{1}{\sqrt{Z}} \sum_n e^{-\frac{\beta}{2} E_n}|n\rangle \otimes |n\rangle. \tag{2.26}$$

The choice $t_L = -t_R$ is time-independent, and corresponds to the ∂_t Killing vector of the geometry.

3 Volume for Janus AdS$_3$

In this section we apply the CV conjecture to the Janus AdS$_3$ geometry. We consider an extremal spacelike codimension-one slice attached to the boundary and we evaluate the induced volume. Since this geometric object extends all the way to the boundary, the corresponding holographic complexity will be divergent and it is necessary to regularize the UV modes. In the case of entanglement entropy, divergences arise due to the arbitrarily short correlations between degrees of freedom on each side of the entangling surface. The leading divergence scales with the area law and either the finite term (in odd spacetime dimensions) or the coefficient of the logarithmic divergence (in even spacetime dimensions) have a universal interpretation which is not sensitive to the ambiguities in the choice of the regulator. In the case of complexity, the outcome of a similar classification is a leading divergence proportional to the boundary volume of the time slice, and a set of subleading terms defined in terms of integrals over the same slice [30].

However, this structure may change when defects, interfaces, or boundaries are present, and it is interesting to understand how the structure gets modified. This problem has already been addressed in some specific cases [51–53]. In this section we will study the UV divergences of the AdS$_3$ Janus geometry. This analysis will clarify the universality of UV divegences in spacetimes containing a codimension-one object by comparing with the Randall-Sundrum model [51] or with the case of a boundary CFT holographically described by an end of the world brane [52, 53].

In the calculation of the volume, an IR regulator is also needed in order to get a finite result. To deal with this divergence, a possibility could be to introduce an IR cutoff at some constant value of the Fefferman-Graham (FG) coordinates. This approach is not very practical for the Janus geometry, as the FG coordinates are known just as an expansion nearby the boundary. In our case, it is more convenient to use the related concept of subregion complexity as an IR regulator.

Subregion volume complexity [10] is from the bulk perspective defined as the volume of an extremal slice limited by a constant time subregion on the boundary and the corresponding HRT surface. The precise meaning of subregion complexity in the dual CFT is still an open question. Some proposals, such as fidelity, purification complexity and basis complexity, were discussed in [10, 35]. In any event, the HRT surface defining the subregion

volume can effectively be used as an infrared regulator: the total complexity will then be defined as the limit in which the subregion covers the entire boundary. In the case of the Janus geometries under consideration in this section, the spacetime is $(2 + 1)$-dimensional and then the RT surface is a geodesic.

In section 3.1, we discuss the time independence of the volume of the Janus AdS geometry. In section 3.2 three different prescriptions to regulate the UV divergences of the extremal volume are described; these regularization only differ by finite terms. In section 3.3 we compute the Janus AdS$_3$ volume, using the single cutoff regularization; in sections 3.4 and 3.5 we will discuss how the computation is modified using the FG and the double cutoff regularizations. We will show that these regularization prescriptions differ only by a finite term. In section 3.6 we will compare the result with the one found in other AdS defect geometries.

3.1 Time independence of the volume in the Janus AdS$_3$ geometry

We want to show that it is not restrictive to study the CV conjecture in the Janus AdS$_3$ background using a time slice at constant boundary time. One could be tempted to assign different time arrows on each of the two $y = \pm\infty$ boundaries (as customary for the left and right side of the Kruskal diagram). However, this is not consistent because the two boundaries are not causally disconnected. We are then forced to evolve the time in a unique way according to the asymptotic Killing vector of the metric. This forces us to take the boundary condition of the extremal volume at constant time t. The discussion also applies to the HRT surface associated to the subregion, which is also time independent.

Let us now show that the whole solution is at constant t. We parametrize the codimension-one slice expressing the time as a function $t(y, z)$. From the metric in eq. (2.3), the volume functional is

$$\mathcal{V} = L^2 \int dz \, dy \, \mathcal{L} \,, \qquad \mathcal{L} = \frac{\sqrt{f(y)}}{z} \sqrt{1 - (\partial_y t)^2 - \frac{f(y)}{z^2} \, (\partial_z t)^2} \,. \qquad (3.1)$$

The $t = t_0$ function, where t_0 is a constant, is a solution of the Euler-Lagrange equation. Moreover, this solution has the property to maximize the volume functional.

3.2 UV regularizations for the volume

The volume is divergent and needs a regularization by an UV cutoff. The choice of this cutoff is a delicate issue in Janus geometries, due to the presence of subtleties with the Fefferman-Graham (FG) coordinates. Nearby the defect, there is a region where the FG patch is not well-defined and the UV cutoff surface is ambiguous. To overcome this problem, we will use three different regularization prescriptions and we will show that they only differ by finite terms. Each regularization is equally valid to describe the relevant physics of the system.

We generically consider an interface CFT described by a codimension-one defect embedded in a AdS$_{d+1}$ bulk geometry, whose isometries get reduced from the conformal group SO$(d, 2)$ to the subgroup SO$(d - 1, 2)$. The natural way to parametrize this geometry is to

perform a slicing of spacetime in terms of AdS_d slices. The metric takes the form [61]

$$ds^2 = L^2 \left(A^2(y) ds^2_{\mathrm{AdS}_d} + \rho^2(y) dy^2 \right) , \qquad (3.2)$$

with y being a non-compact coordinate such that when $y \to \pm\infty$ we have the asymptotic behaviour

$$A(y) \to \frac{L_\pm}{2} e^{\pm y \pm c_\pm} , \qquad \rho(y) \to 1 . \qquad (3.3)$$

Here $L_\pm$ and $c_\pm$ are constants (which can take different values at the boundaries $y = \pm\infty$), and we are assuming that there is not any other internal direction in the spacetime. We parametrize the AdS_d slices using Poincaré coordinates

$$ds^2_{\mathrm{AdS}_d} = \frac{1}{z^2} \left(dz^2 - dt^2 + d\vec{x}^2_{d-2} \right) , \qquad (3.4)$$

where (t, z) are the time and radial coordinates on each slice and $\vec{x}$ collects all the other orthogonal directions. In the following, we will use three regularization techniques inspired by the similar discussion for the free energy [62] and the entanglement entropy [61, 63]. In all the computations of this section, the volume will be determined from

$$\mathcal{V} = \int dz \int dy \int d\vec{x} \, \sqrt{h} , \qquad (3.5)$$

where $\sqrt{h}$ is the determinant of the induced metric. The integration along the orthogonal spatial directions $\vec{x}$ is usually trivial, while the part along the (y, z) coordinates contains the relevant information about the defect.

The three different regularization that we will consider are:

- **Fefferman-Graham regularization.** The Fefferman-Graham (FG) form of the metric is

$$ds^2 = \frac{L^2}{\xi^2} \left[d\xi^2 + g_1(\xi/\eta) \left(-dt^2 + d\vec{x}^2 \right) + g_2(\xi/\eta) \, d\eta^2 \right] , \qquad (3.6)$$

  where ξ is a radial coordinate for the asymptotic AdS region in Poincaré coordinates, η is a field theory direction orthogonal to the defect, and g_1, g_2 are two opportune functions, such that the original metric (3.2) with slicing (3.4) is equivalent to (3.6) with a suitable change of coordinates $(z, y) \to (\xi, \eta)$. We perform an expansion of eq. (3.6) such that the asymptotic metric reads

$$ds^2 = \frac{L^2}{\xi^2} \left(d\xi^2 + d\eta^2 + d\vec{x}^2 - dt^2 + \mathcal{O}(\xi) \right) . \qquad (3.7)$$

  The natural prescription to regularize divergences using the FG form of the metric is to introduce a UV cutoff by cutting the spacetime with the surface located at $\xi = \delta$, and expand all the results in a series around $\delta = 0$. The problem of this procedure is that in the region where $\xi/\eta \gg 1$, the FG expansion breaks down and the coordinates (ξ, η) are ill-defined [57].

  For this reason, the defect geometry is characterized by the existence of two patches, defined away from the region of the defect on the left and right sides of the spacetime,
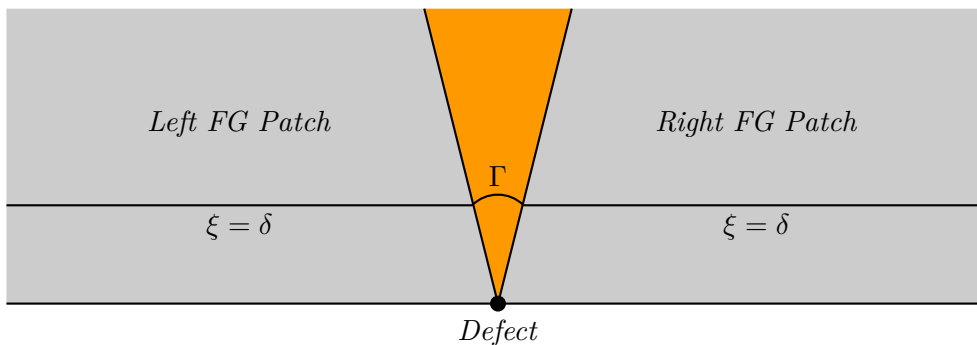
Figure 5. Interpolation between two FG patches with a continuous curve Γ.

where the FG expansion is valid: we call them FG patches (see figure 5.) We do not have access to a natural UV cutoff in the middle region closer to the defect. To overcome the problem, the original proposal from [61] is to interpolate the cutoff determined by requiring $\xi = \delta$ in the left and right FG patches with an arbitrary curve in the middle region. The only constraint is that the curve should be continuous at the value $y = y_0$ where the FG expansion breaks down. The corresponding curve is pictorially represented in figure 5.

This method was later applied to the calculation of complexity in [51], with the additional requirement that the interpolation is smooth, i.e., the curves in the middle region are perpendicular to the surface which delimits the FG patches. We will discuss the details of this method in section 3.4.

- **Single cutoff regularization.** This technique [62] is inspired by the Fefferman-Graham method, but has the advantage to not introduce any arbitrary interpolating curve in the middle region. Instead, it uses the FG map to induce a minimal value on the z coordinate, in such a way that the integration does not reach the region $z \to 0$ where the expansion breaks down. We explain how the procedure works starting from AdS_{d+1}, which can be written using the slicing (3.2) choosing $A(y) = \cosh y$ and $\rho(y) = 1$. In this case, the coordinate transformation which brings the metric to the FG form in eq. (3.6) is

$$\eta = z \tanh y, \qquad \xi = \frac{z}{\cosh y}. \tag{3.8}$$

If we locate the UV cutoff at the surface $\xi = \delta$, we get the condition

$$\delta = \frac{z}{\cosh y}, \tag{3.9}$$

which selects a maximal value of $y = y^*(z)$ for the first non-trivial integration in eq. (3.5). Reversing this formula gives a constraint on the minimal value of the integration along z, determined by

$$z_{\min} = \delta \min_{y \in \mathbb{R}} (\cosh y) = \delta. \tag{3.10}$$

In this way, we observe that the choice of a single cutoff δ from the FG expansion restricts the integration along both the (y, z) coordinates and regularizes the volume.

In the presence of a defect, the procedure is the same, except that the conditions determined from the FG form of the metric get modified to

$$\delta = \frac{z}{A(y)}, \qquad z_{\min} = \delta \min_{y \in \mathbb{R}} [A(y)].$$ (3.11)

We apply this technique in section 3.3.

- **Double cutoff regularization.** The previous technique regularizes all the integrals with the choice of a single UV cutoff inspired by the FG expansion. On the other hand, we can consider two different cutoffs for the each of the directions (y, z). This method [63] is based on the observation that, after the subtraction of the vacuum geometry, we should obtain a holographic quantity intrinsic to the defect: for this reason, a natural cutoff can be imposed on the AdS_d slicing at $z = \delta$, instead of selecting the asymptotic radial direction in the AdS_{d+1} bulk geometry. This choice by itself is not sufficient to regularize the full integral (3.5), since the metric factor $A(y)$ is still singular at infinity: for this reason we also determine a maximum value of y where the integration ends by requiring

$$A(y) = \frac{1}{\varepsilon}.$$ (3.12)

Notice that while the δ cutoff has physical relevance as it regularizes the intrinsic contribution from the defect, the ε cutoff is a mathematical artifact introduced at intermediate steps, and the result should therefore be ε-independent. As a consequence of this, we are allowed to remove the ε cutoff at the end of the computation. We apply this procedure in section 3.5.

3.3 Single cutoff regularization

We will consider a symmetric region of radius $l/2$ centered on the defect in Janus AdS_3 and we will compute its subregion complexity. The total complexity can be defined as the $l \to \infty$ limit of this result, with the length l playing the role of IR regulator.

The interval is located at the FG radial coordinate $\xi = 0$ and placed symmetrically along the orthogonal direction to the interface, i.e., $\eta \in [-\frac{l}{2}, \frac{l}{2}]$. There is an ambiguity in the regularization of the UV divergences: we can either put the subregion on the cutoff surface $\xi = \delta$ and build the corresponding HRT surface, or we can put the interval on the real boundary $\xi = 0$ and then cut the HRT surface with the line at $\xi = \delta$. Since the difference between the two cases vanishes in the $\delta \to 0$ limit, we will only focus on the latter case.

As pointed out in [63], on a fixed time slice there is a particular simple class of geodesics for the Janus geometry given by curves at constant z. Using the FG expansion in eq. (2.15) and putting the boundary conditions $\xi = 0$ and $\eta = \frac{l}{2}$, we determine the constant $\bar{z}$ value where the surface is located:

$$\bar{z} = \frac{l}{2}.$$ (3.13)

The prescription for the extremal volume tells us to consider a solution at $t = 0$ anchored at the boundary and delimited by the HRT surface.

The UV divergencies will be regularised according to the single cutoff prescription described in section 3.2. The correspondence between the generic form (3.2) of the metric with a conformal defect and the Janus background is

$$A^2(y) = f(y), \qquad \rho(y) = 1, \qquad L_\pm^2 = \sqrt{1 - 2\gamma^2}, \qquad c_\pm = 0. \tag{3.14}$$

In this way the requirement in eq. (3.11) to regularize the UV divergences becomes

$$\frac{z}{\sqrt{f(y)}} = \delta. \tag{3.15}$$

This single condition identifies both a maximum value of the coordinate $y = y^*(z)$, obtained by inverting the previous expression, and a minimum value of the coordinate $z = z_{\min}$, determined from the second identity in eq. (3.11). Concretely, they are given by

$$y^*(z) = f^{-1}\left(\frac{z^2}{\delta^2}\right), \qquad z_{\min} = a\,\delta, \qquad a^2 = f(0) = \frac{1 + \sqrt{1 - 2\gamma^2}}{2}. \tag{3.16}$$

The integral which computes the subregion volume in eq. (3.5) takes the form

$$\mathcal{V}(l, \gamma) = 2L^2 \int_{z_{\min}}^{\bar{z}} \frac{dz}{z} \int_0^{y^*(z)} dy \sqrt{f(y)}. \tag{3.17}$$

Changing variables into

$$\tau = \frac{f(y)}{a^2}, \qquad \zeta = \frac{z^2}{a^2\delta^2}, \qquad \bar{\zeta} = \frac{\bar{z}^2}{a^2\delta^2}, \tag{3.18}$$

we can express the integral as

$$\begin{aligned}
\mathcal{V}(l, \gamma) &= \frac{L^2 a^3}{\sqrt{2}} \int_1^{\bar{\zeta}} \frac{d\zeta}{\zeta} \int_1^{\zeta} \frac{\tau^{1/2} d\tau}{\sqrt{\gamma^2 + 2a^2\tau(a^2\tau - 1)}} \\
&= \frac{L^2 a^3}{\sqrt{2}} \int_1^{\bar{\zeta}} d\tau \int_\tau^{\bar{\zeta}} \frac{d\zeta}{\zeta} \frac{\tau^{1/2}}{\sqrt{\gamma^2 + 2a^2\tau(a^2\tau - 1)}}.
\end{aligned} \tag{3.19}$$

It is useful to define

$$m = \frac{1 - \sqrt{1 - 2\gamma^2}}{1 + \sqrt{1 - 2\gamma^2}}, \tag{3.20}$$

which is one of the zeroes of the denominator. Since $0 \leq \gamma \leq 1/\sqrt{2}$, we have $1/\sqrt{2} \leq a \leq 1$ and $0 \leq m \leq 1$. A direct evaluation gives

$$\begin{aligned}
\mathcal{V}(l, \gamma) &= \frac{L^2 a}{2} \int_1^{\bar{\zeta}} \frac{(\log \bar{\zeta} - \log \tau)\, \tau^{1/2}}{\sqrt{(\tau - 1)(\tau - m)}}\, d\tau \\
&= L^2 \left(\frac{l}{\delta} + \eta(\gamma) \log\left(\frac{l}{2a\,\delta}\right) + \chi(\gamma)\right),
\end{aligned} \tag{3.21}$$

where

$$\eta(\gamma) = a\left[\int_1^\infty \tau^{1/2}\left(\frac{1}{\sqrt{(\tau-1)(\tau-m)}} - \frac{1}{\tau}\right)d\tau - 2\right] = 2a\left(\mathbb{K}(m) - \mathbb{E}(m)\right), \qquad (3.22)$$

$$\chi(\gamma) = a\left[-2 - \frac{1}{2}\int_1^\infty \tau^{1/2}\log\tau\left(\frac{1}{\sqrt{(\tau-1)(\tau-m)}} - \frac{1}{\tau}\right)d\tau\right]. \qquad (3.23)$$

The complexity of the total space can be obtained from the $l \to \infty$ limit of eq. (3.21).

To compute the contribution to the volume arising purely from the defect, we need to subtract the result from AdS$_3$ space. This amounts to put $\gamma = 0$ in the previous result, giving

$$\eta(0) = 0, \qquad \chi(0) = -\pi. \qquad (3.24)$$

For a cross-check, we can perform directly the AdS$_3$ calculation

$$y^* = \text{arccosh}\left(\frac{z}{\delta}\right), \qquad z_{\min} = \delta, \qquad (3.25)$$

and the integral computing the volume is

$$\mathcal{V}(l,0) = 2L^2\int_\delta^{\bar{z}}\frac{dz}{z}\int_0^{\text{arccosh}(z/\delta)}dy\,\cosh y = L^2\left(\frac{l}{\delta} - \pi\right), \qquad (3.26)$$

which is consistent with eq. (3.24).

The difference between the regularised volumes of the Janus geometry and AdS$_3$ is

$$\Delta\mathcal{V}(l,\gamma) \equiv \mathcal{V}(l,\gamma) - \mathcal{V}(l,0) = L^2\left(\eta(\gamma)\log\left(\frac{l}{2a\,\delta}\right) + \chi(\gamma) + \pi\right). \qquad (3.27)$$

The only divergence in eq. (3.27) is logarithmic, which is interpreted as the contribution from the defect, and it is proportional to the function $\eta(\gamma)$. Note that for small γ

$$\eta(\gamma) \approx \frac{\pi}{4}\gamma^2, \qquad (3.28)$$

and that η is divergent for $\gamma \to 1/\sqrt{2}$, which corresponds to the linear dilaton limit. A plot of $\eta(\gamma)$ is shown in figure 6.

Note that the l-dependent part of eq. (3.27) is proportional to the entanglement entropy of the segment without the defect, i.e.,

$$S_{\text{AdS}} = \frac{c}{3}\log\left(\frac{l}{\delta}\right). \qquad (3.29)$$

3.4 Fefferman-Graham regularization

This method consists in using the FG form of the metric in eq. (3.6) to identify a UV cutoff in terms of the proper radial coordinate near the boundary. In particular, it is required that when $\xi \to 0$ the asymptotic behaviour respects the limits

$$g_1(\xi/\eta) \to 1, \qquad g_2(\xi/\eta) \to 1. \qquad (3.30)$$
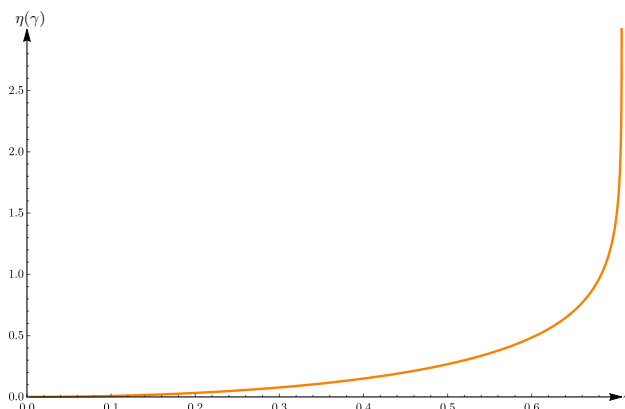
Figure 6. Plot of $\eta(\gamma)$ as defined in eq. (3.22), which is the coefficient of the log divergencies due to the defect.

The change of coordinates from (y, z) to (ξ, η) breaks down when $\xi/\eta \gg 1$, which corresponds to approaching the interface. This condition is equivalent to the statement that there exists a value of $y = y_0$ such that the FG expansion breaks down. Since $f(y)$ is a monotonically increasing function in the region $y \geq 0$, this equivalently implies that there exists a value $b \geq 1$ such that

$$A(y_0) = b\, A(0)\,, \tag{3.31}$$

where $A(y)$ was introduced in eq. (3.2). This criterion selects a particular $y = y_0$ such that

$$y_0 = A^{-1}(bA(0))\,. \tag{3.32}$$

There exist universal quantities that do not depend on the choice of the curve connecting the two FG patches [61]. For this reason, in the region where $y \in [-y_0, y_0]$ we can introduce an arbitrary curve interpolating between the two regions. As proposed in [51], we will select an interpolating curve connecting smoothly the two patches. In the following, we show that this prescription gives the same result as the single cutoff method applied in section 3.3, except for the finite part.

Integration in the FG patches. We consider the FG expansion defined in eq. (2.15) with a UV cutoff located at $\xi = \delta$ and the condition $y \gg 1$. In this way we find

$$\frac{\delta}{z} = \frac{1}{\sqrt{f(y)}}\,, \quad \Rightarrow \quad y^* = \frac{1}{2}\operatorname{arccosh}\left(\frac{\frac{2z^2}{\delta^2} - 1}{\sqrt{1 - 2\gamma^2}}\right)\,, \tag{3.33}$$

which is equivalent to the single cutoff prescription (3.11) after using the identification in (3.14). According to eq. (3.32), we determine the minimal value of $y = y_0$ such that the FG expansion is valid by solving

$$\sqrt{f(y_0)} = a\, b \quad \Rightarrow \quad y_0 = \frac{1}{2}\operatorname{arccosh}\left(\frac{2a^2b^2 - 1}{\sqrt{1 - 2\gamma^2}}\right)\,. \tag{3.34}$$

Therefore, the integration in the FG patch region is given by

$$\mathcal{V}^1_{\mathrm{FG}}(l,\gamma) = 2L^2 \int_{z^{\mathrm{FG}}_{\min}}^{\bar{z}} \frac{dz}{z} \int_{y_0}^{y^*(z)} dy \sqrt{f(y)} \,, \tag{3.35}$$

where $\bar{z}$ was defined in eq. (3.13), and we put a symmetry factor of 2 due to the symmetry of the problem. The minimal value $z = z^{\mathrm{FG}}_{\min}$ is determined as

$$z^{\mathrm{FG}}_{\min} = \min_{y \in [y_0, y^*]} \left(\sqrt{f(y)} \right) \delta = a\, b\, \delta \,, \tag{3.36}$$

where we used the fact that in a single FG patch the function $f(y)$ is monotonically increasing. Notice that this value of $z^{\mathrm{FG}}_{\min}$ differs from $z_{\min}$ in eq. (3.16) (determined for the single cutoff prescription) only by the factor b.

Interpolation in the middle region. Now we consider the middle region where we do not have access to a FG expansion. We show that the surfaces at constant y and the ones at constant z are orthogonal to each others. Since the normal one-forms to such surfaces are given by

$$\mathbf{v} = dy \,, \qquad \mathbf{w} = dz \,, \tag{3.37}$$

one can easily show that $\mathbf{v} \cdot \mathbf{w} = 0$. Even though the coordinates (ξ, η) are not defined in the middle region, the original variables (y, z) are still valid. According to [51], the curve interpolating the FG patches should be chosen perpendicular to the surface located at $y = y_0$. On the time slice $t = 0$, this condition selects curves at constant z.

The integral in this region reads

$$\mathcal{V}^2_{\mathrm{FG}}(l,\gamma) = 2L^2 \int_{z^{\mathrm{FG}}_{\min}}^{\bar{z}} \frac{dz}{z} \int_0^{y_0} dy \sqrt{f(y)} \,. \tag{3.38}$$

The total volume is

$$\mathcal{V}_{\mathrm{FG}}(l,\gamma) \equiv \mathcal{V}^1_{\mathrm{FG}}(l,\gamma) + \mathcal{V}^2_{\mathrm{FG}}(l,\gamma) = 2L^2 \int_{z^{\mathrm{FG}}_{\min}}^{\bar{z}} \frac{dz}{z} \int_0^{y^*} dy \sqrt{f(y)} \,, \tag{3.39}$$

which is exactly the integral (3.17) that we evaluated for the single cutoff prescription, except that now we integrate from $z^{\mathrm{FG}}_{\min} \geq z_{\min}$. Subtracting vacuum AdS_3, the result is

$$\Delta \mathcal{V}_{\mathrm{FG}}(l,\gamma) = L^2 \left[\eta(\gamma) \log \left(\frac{l}{2a\, b\, \delta} \right) + \chi(\gamma) + \pi \right] \,. \tag{3.40}$$

The result, up to a finite term, coincides with eq. (3.27). This procedure also shows that the value $y = y_0$ where the FG patch ends does not play any special role.

3.5 Double cutoff regularization

Here we repeat the calculation of the previous section using the double cutoff prescription. Following the procedure described in section 3.2, we take one cutoff at $z = \delta$, whereas the other one is determined by

$$f(y) = \frac{1}{\varepsilon^2} \,. \tag{3.41}$$

Solving the previous equations for $y = y^*$, we find

$$y^*(\varepsilon) = f^{-1}\left(\frac{1}{\varepsilon^2}\right) . \tag{3.42}$$

This value is the same as the one in eq. (3.16), once we identify $\varepsilon = \delta/z$. The main difference using this method is that ε does not depend on z. Thus, the two integrals defining the volume are independent and factorize. Then, the extremal volume for the subregion is given by

$$\mathcal{V}(l,\gamma) = 2L^2 \int_\delta^{\bar{z}} \frac{dz}{z} \int_0^{y^*(\varepsilon)} dy \sqrt{f(y)} . \tag{3.43}$$

Following the analysis in section 3.3 and performing the change of variables

$$\tau = \frac{f(y)}{a^2} , \tag{3.44}$$

we obtain

$$\mathcal{V}(l,\gamma) = L^2 a \log\left(\frac{\bar{z}}{\delta}\right) \int_1^{1/(a^2\varepsilon^2)} d\tau \sqrt{\frac{\tau}{(\tau-1)(\tau-m)}} . \tag{3.45}$$

A direct evaluation gives

$$\mathcal{V}(l,\gamma) = L^2 \left(\eta(\gamma) + \frac{2}{\varepsilon}\right) \log\left(\frac{\bar{z}}{\delta}\right) , \tag{3.46}$$

where $\eta(\gamma)$ is defined in eq. (3.22). Subtracting the volume of pure AdS$_3$ space which is given by

$$\mathcal{V}(l,0) = L^2 \frac{2}{\varepsilon} \log\left(\frac{\bar{z}}{\delta}\right) + \mathcal{O}(\varepsilon) , \tag{3.47}$$

we get the contribution to the volume from the defect

$$\Delta\mathcal{V}(l,\gamma) = L^2 \eta(\gamma) \log\left(\frac{l}{2\,\delta}\right) + \mathcal{O}(\delta) . \tag{3.48}$$

We observe that the dependence on ε disappears after the subtraction, consistently with the non-physical relevance of this cutoff [63]. The remaining logarithmic divergence matches with the single cutoff calculation in eq. (3.27), up to finite parts.

3.6 Comparison with other defect geometries

In this section, we investigated subregion volume complexity for an interval of length l centered around the Janus interface, using three different regularizations. We found that the increment of subregion complexity compared to the vacuum CFT is

$$\Delta\mathcal{C}(l,\gamma) = \frac{2}{3} c\, \eta(\gamma) \log\left(\frac{l}{\delta}\right) + \text{finite terms} , \tag{3.49}$$

where c is the CFT central charge and $\eta(\gamma)$ is

$$\eta(\gamma) = 2\sqrt{\frac{1+\sqrt{1-2\gamma^2}}{2}} \left[\mathbb{K}(m) - \mathbb{E}(m)\right] , \qquad m = \frac{1-\sqrt{1-2\gamma^2}}{1+\sqrt{1-2\gamma^2}} . \tag{3.50}$$

A plot of $\eta(\gamma)$ is shown in figure 6. We can contrast this with the ground state degeneracy g of the Janus solution computed in [43], given by

$$\Delta S = \log g = \frac{c}{6}\kappa(\gamma), \qquad \kappa(\gamma) = \log \frac{1}{\sqrt{1 - 2\gamma^2}}. \qquad (3.51)$$

The value $0 \leq \gamma < \frac{\sqrt{2}}{2}$ parameterizes the excursion of the dilaton between the two sides of the interface, which diverges for $\gamma \to \frac{\sqrt{2}}{2}$.

It is interesting to compare $\Delta\mathcal{C}$ for the Janus interface with recent results found for other defect geometries, namely:

- the AdS$_3$ Randall-Sundrum model, where the contribution to complexity coming from the defect, evaluated in [51], is

$$\Delta\mathcal{C}(l, y^*) = \frac{2}{3}c\,\eta_{\mathrm{RS}} \, \log\frac{l}{\delta} + \text{finite terms}, \qquad \eta_{\mathrm{RS}} = 2\sinh y^*, \qquad (3.52)$$

where the parameter $0 \leq y^* < \infty$ is related to the brane tension λ by

$$\lambda = \frac{\tanh y^*}{4\pi G L}. \qquad (3.53)$$

In this case, the defect boundary entropy [43] is

$$\Delta S = \log g = \frac{c}{6}\kappa_{\mathrm{RS}}, \qquad \kappa_{\mathrm{RS}} = 2y^*; \qquad (3.54)$$

- the BCFT model. Complexity was studied in [52, 53] and a similar scenario for an holographic Kondo model was investigated in [47]. For the three-dimensional case, the subregion volume complexity reads

$$\Delta\mathcal{C}(l, \alpha) = \frac{2}{3}c\,\eta_{\mathrm{BCFT}} \, \log\frac{l}{\delta} + \text{finite terms}, \qquad \eta_{\mathrm{BCFT}} = \cot\alpha, \qquad (3.55)$$

where the parameter $0 < \alpha \leq \frac{\pi}{2}$ is related to the brane tension T as follows

$$T = \frac{\cos\alpha}{L}. \qquad (3.56)$$

The defect boundary entropy [45, 46] is

$$\Delta S = \log g = \frac{c}{6}\kappa_{\mathrm{BCFT}}, \qquad \kappa_{\mathrm{BCFT}} = \log\left(\cot\frac{\alpha}{2}\right). \qquad (3.57)$$

We conclude that:

1. the leading divergence in $\Delta\mathcal{C}$ is always logarithmic, with a positive coefficient η that is a function of the deformation parameter of the model;

2. in all three cases, the log divergence in $\Delta\mathcal{C}$ is not related in any universal way to the defect boundary entropy ΔS. Nonetheless, the two quantities share a similar behavior, that is, they diverge for the same critical value;
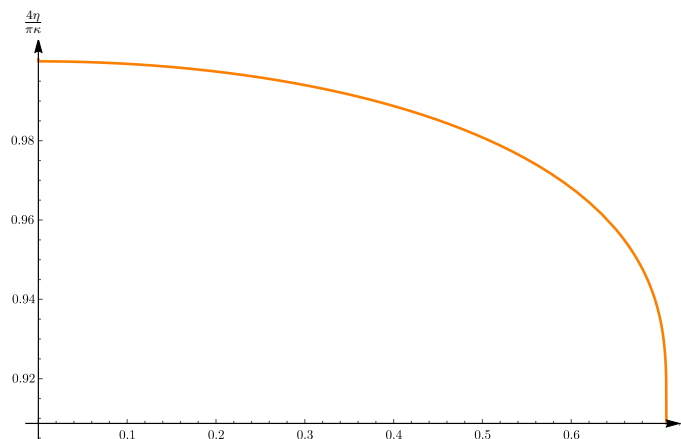
Figure 7. Plot of $4\eta/(\pi\kappa)$ as a function of γ, see eq. (3.51).

3. for small values of the deformation parameters, in all the models η/κ is of order 1, i.e.,

$$\frac{\eta(\gamma)}{\kappa(\gamma)} = \frac{\pi}{4}\,, \qquad \frac{\eta_{\mathrm{RS}}}{\kappa_{\mathrm{RS}}} = \frac{\eta_{\mathrm{BCFT}}}{\kappa_{\mathrm{BCFT}}} = 1\,; \tag{3.58}$$

4. in the Janus case η/κ remains very close to $\frac{\pi}{4}$ for the whole range of the deformation parameter γ (see figure 7). On the contrary, in the other two models $\eta \gg \kappa$ close to the critical values $y^* \to \infty$ and $\alpha \to 0$.

4 Volume of the static Janus BTZ black hole

In the finite temperature case, it is interesting to consider the thermal complexity of formation [64], which corresponds to the additional complexity needed to prepare the thermofield double state starting from two copies of unentangled vacuum CFTs. We study this quantity for the Janus interface. In the CV conjecture, this corresponds to the volume of the initial time slice of the Kruskal extension of the static Janus BTZ subtracted by twice the Janus AdS contribution.

4.1 Single cutoff regularisation

In this section we compute the subregion complexity for a symmetric interval with length l centered around the defect of the static Janus BTZ geometry at vanishing boundary time. The metric is

$$ds^2 = L^2 \left[dy^2 + f(y) \left(-\frac{(w^2-1)r_h^2}{L^4}dt^2 + \frac{dw^2}{w^2-1} \right) \right], \tag{4.1}$$

which is obtained by substituting the Rindler-like metric (2.21) in (2.20), and performing the μ-to-y change of variable $d\mu = dy/\sqrt{f(y)}$.

The HRT surface on a constant time slice lies at a constant value $w = \bar{w}$ [60]. We locate the interval along the coordinate $x \in [-\frac{l}{2}, \frac{l}{2}]$ orthogonal to the defect and on the

real boundary parametrized by $r = \infty$. The value of $\bar{w}$ can be obtained by combining the two equations (2.24) with $r = \infty$, $x = l/2$ and solving for $\bar{w}$, which gives

$$\bar{w} = \coth\left(\frac{lr_h}{2L^2}\right) \tag{4.2}$$

The UV divergencies are regularized with the single cutoff prescription presented in section 3.2. The natural choice of cutoff is found by performing a FG expansion of the metric to relate the asymptotic behavior of the deformed BTZ black hole with the non-deformed counterpart. Such asymptotic behaviour is identified by

$$\frac{r}{r_h} \simeq \sqrt{(w^2 - 1)f(y) + 1}\,. \tag{4.3}$$

The cutoff surface determined by the FG expansion at $r = L^2/\delta$ induces the following value of y coordinate

$$y^*(w) = \frac{1}{2}\mathrm{arcosh}\left(\frac{2 - \hat{\delta}^2\,(w^2 + 1)}{\hat{\delta}^2\,(w^2 - 1)\,\sqrt{1 - 2\gamma^2}}\right)\,, \qquad \hat{\delta} = \frac{r_h\delta}{L^2}\,. \tag{4.4}$$

This in turn induces a cutoff in the w coordinate, which is found by maximizing the inverse of the previous function

$$w(y) = \sqrt{\frac{2/\hat{\delta}^2 + \sqrt{1 - 2\gamma^2}\cosh(2y) - 1}{\sqrt{1 - 2\gamma^2}\cosh(2y) + 1}}\,, \tag{4.5}$$

with respect to y. The maximum occurs at $y = 0$, and thus

$$w_{\max} = \sqrt{\frac{2/\hat{\delta}^2 + \sqrt{1 - 2\gamma^2} - 1}{\sqrt{1 - 2\gamma^2} + 1}}\,. \tag{4.6}$$

This UV cutoff is the analog of $z_{\min}$ in the Janus AdS$_3$ case, see eq. (3.16).

The extremal volume (3.5) for the static Janus BTZ geometry reads

$$\mathcal{V}(l, \gamma) = 2L^2 \int_{\bar{w}}^{w_{\max}} dw \int_0^{y^*(w)} dy \sqrt{\frac{f(y)}{w^2 - 1}}\,. \tag{4.7}$$

After performing the following change of variables

$$\tau = \frac{f(y)}{a^2}\,, \qquad z = \frac{1 - \hat{\delta}^2}{a^2\hat{\delta}^2(w^2 - 1)}\,, \qquad \bar{z} = \frac{1 - \hat{\delta}^2}{a^2\hat{\delta}^2(\bar{w}^2 - 1)}\,, \tag{4.8}$$

the integral takes the form

$$\begin{aligned}
\mathcal{V}(l, \gamma) &= \frac{L^2 a}{2} \int_1^{\bar{z}} \frac{dz}{\sqrt{1 + \alpha^2 z}} \int_1^z d\tau \sqrt{\frac{\tau}{(\tau - 1)(\tau - m)}} \\
&= \frac{L^2 a}{2} \int_1^{\bar{z}} d\tau \sqrt{\frac{\tau}{(\tau - 1)(\tau - m)}} \int_\tau^{\bar{z}} \frac{dz}{z\sqrt{1 + \alpha^2 z}}\,,
\end{aligned} \tag{4.9}$$

where

$$\alpha = \frac{a\,\hat{\delta}}{\sqrt{1 - \hat{\delta}^2}}\,. \tag{4.10}$$

The integration over z yields three kind of terms, according to which we split the extremal volume as

$$\mathcal{V}(l,\gamma) = \mathcal{V}_1 + \mathcal{V}_2 + \mathcal{V}_3\,, \tag{4.11}$$

where

$$
\begin{aligned}
\mathcal{V}_1 &= L^2 a \int_1^{\bar{z}} d\tau \, \log\left(1 + \sqrt{1 + \alpha^2 \tau}\right) \sqrt{\frac{\tau}{(\tau-1)(\tau-m)}}\,, \\
\mathcal{V}_2 &= -\frac{L^2 a}{2} \int_1^{\bar{z}} d\tau \, \log\tau \, \sqrt{\frac{\tau}{(\tau-1)(\tau-m)}}\,, \\
\mathcal{V}_3 &= -L^2 a \int_1^{\bar{z}} d\tau \, \log\left(\frac{1 + \sqrt{1 + \alpha^2 \bar{z}}}{\sqrt{\bar{z}}}\right) \sqrt{\frac{\tau}{(\tau-1)(\tau-m)}}\,.
\end{aligned}
\tag{4.12}
$$

These integrals can be evaluated explicitly following similar steps as in section 3.3. The result is

$$\mathcal{V}(l,\gamma) = L^2\left(\frac{l}{\delta} + \eta(\gamma)\log\left[\frac{2L^2}{a\,\delta\,r_h}\tanh\left(\frac{lr_h}{4L^2}\right)\right] + \chi(\gamma)\right) + \mathcal{O}(\delta)\,, \tag{4.13}$$

where $\eta(\gamma)$ and $\chi(\gamma)$ were defined in eq. (3.22).

In absence of the interface (for $\gamma = 0$) the volume is still given by the AdS$_3$ result in eq. (3.26). This is due to the fact that subregion volume complexity in the BTZ background does not depend on temperature and it is topologically protected by the Gauss-Bonnet theorem [32]. On the other hand, in the case of the Janus interface subregion complexity depends on the temperature. In the small temperature regime $r_h l \ll 1$, we recover the Janus AdS result in eq. (3.21).

Using the expression for temperature and the central charge

$$T = \frac{r_h}{2\pi L^2}\,, \qquad c = \frac{3L}{2G}\,, \tag{4.14}$$

we get that the subregion complexity, in terms of field theory quantities, is

$$\mathcal{C}(T,l,\gamma) = \frac{\mathcal{V}(l,\gamma)}{LG} = \frac{2}{3}c\left(\frac{l}{\delta} + \eta(\gamma)\log\left[\frac{1}{\pi a T\delta}\tanh\left(\frac{\pi l T}{2}\right)\right] + \chi(\gamma)\right)\,. \tag{4.15}$$

The temperature dependence of the volume complexity is

$$\Delta\mathcal{C}(T,l,\gamma) \equiv \mathcal{C}(T,l,\gamma) - \mathcal{C}(0,l,\gamma) = \frac{2}{3}c\,\eta(\gamma)\Phi(Tl) \tag{4.16}$$
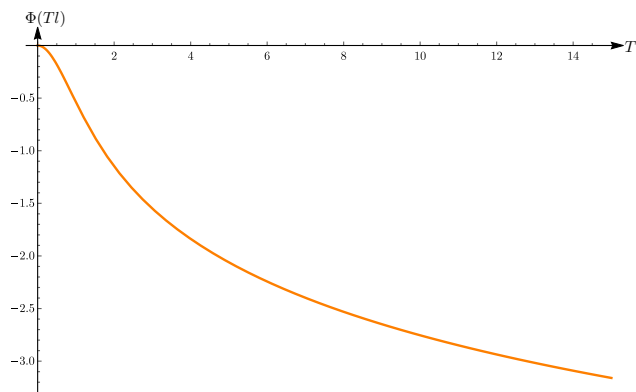
where

$$\Phi(Tl) = \log\left[\frac{2}{\pi l T}\tanh\left(\frac{\pi l T}{2}\right)\right]\,. \tag{4.17}$$

At zero temperature, the contribution of the defect to $\mathcal{C}(0,l,\gamma)$ is proportional to the entanglement entropy of the segment without defect. However, the proportionality is spoiled at finite temperature. In fact, the BTZ entanglement entropy for a segment of length l is

$$S_{\text{BTZ}}(T,l) = \frac{c}{3}\log\left[\frac{2L^2}{r_h\delta}\sinh\left(\frac{lr_h}{2L^2}\right)\right] = \frac{c}{3}\log\left[\frac{1}{\pi T\,\delta}\sinh\left(\pi T l\right)\right]\,, \tag{4.18}$$

Figure 8. Plot of $\Phi(Tl)$ in eq. (4.17), which gives the temperature dependence of the complexity of the interface.

which is an increasing function of T, while $\Delta\mathcal{C}(l,\gamma)$ is a decreasing function of T (see figure 8).

Taking into account the two sides of the Kruskal diagram, the complexity of formation $\mathcal{C}_F$ of the static Janus BTZ starting from the Janus AdS$_3$ background is given by the $l \gg 1/T$ limit of $2\Delta\mathcal{C}$, that is,

$$\mathcal{C}_{\text{Thermal}}^F = \frac{4}{3} c\, \eta(\gamma) \log\left(\frac{2}{\pi l T}\right) , \tag{4.19}$$

where, again, we interpret l as an infrared regulator. In this limit, the complexity of formation is negative. This means that it takes less complexity to form a BTZ black hole in the Janus geometry than the defect alone, starting from empty space.

It is also interesting to consider the complexity of formation of the defect in the BTZ background. In this case, we subtract from eq. (4.15) the $\gamma = 0$ result

$$\mathcal{C}(T,l,\gamma) - \mathcal{C}(T,l,0) = \frac{2}{3} c \left(\eta(\gamma) \log\left[\frac{1}{\pi a T \delta} \tanh\left(\frac{\pi l T}{2}\right) \right] + \chi(\gamma) + \pi \right) . \tag{4.20}$$

Then, considering the $lT \gg 1$ limit and multiplying by an additional factor of two to account for the two sides of the Kruskal diagram, we obtain the complexity of formation of the defect starting from the static BTZ background

$$\mathcal{C}_{\text{Defect}}^F = \frac{4}{3} c \left(\eta(\gamma) \log\left(\frac{1}{\pi a T \delta}\right) + \chi(\gamma) + \pi \right) . \tag{4.21}$$

Notice that, since the volume complexity in the BTZ black hole is topological, the above result can be also interpreted as the complexity of formation of the Janus static BTZ starting from the vacuum AdS$_3$ spacetime.

4.2 Double cutoff regularisation

We compute the subregion volume complexity for the static Janus BTZ geometry by employing the double cutoff regularization. According to this prescription, we directly introduce a physical UV cutoff along the w direction located at $w_{\text{max}} = 1/\hat{\delta}$, but in addition

we regularize the integration along y by requiring eq. (3.41). This constraint induces a maximal value of $y = y^*$ that reads

$$y^* = \frac{1}{2}\text{arccosh}\left(\frac{2 - \varepsilon^2}{\sqrt{1 - 2\gamma^2}\,\varepsilon}\right).$$ (4.22)

Finally, the integration is restricted by the HRT surface, that is located at the constant value $w = \bar{w}$ as determined in eq. (4.2). Collecting these geometrical data, we compute the volume as

$$\mathcal{V}(l, \gamma) = 2L^2 \int_{\bar{w}}^{w_{\max}} dw \int_0^{y^*(\varepsilon)} \sqrt{\frac{f(y)}{w^2 - 1}}.$$ (4.23)

Contrarily to the single cutoff case, the integrations are independent and can be evaluated separately. Using the change of variables $\tau = f(y)/a^2$, we find

$$\begin{aligned}
\mathcal{V}(l, \gamma) &= \frac{L^2 a}{2} \int_{\bar{w}}^{w_{\max}} \frac{dw}{\sqrt{w^2 - 1}} \int_1^{1/(a^2\varepsilon^2)} d\tau \sqrt{\frac{\tau}{(\tau - 1)(\tau - m)}} = \\
&= L^2 \log\left[\frac{1}{\pi T \delta} \tanh\left(\frac{\pi l T}{2}\right)\right]\left(\eta(\gamma) + \frac{2}{\varepsilon}\right) + \mathcal{O}(\delta, \varepsilon).
\end{aligned}$$ (4.24)

The complexity of formation compared to the BTZ black hole background is obtained by subtracting the result in the case $\gamma = 0$. It reads

$$\mathcal{C}(T, l, \gamma) - \mathcal{C}(T, l, 0) = \frac{2}{3} c \left(\eta(\gamma) \log\left[\frac{1}{\pi T \delta} \tanh\left(\frac{\pi l T}{2}\right)\right]\right) + \mathcal{O}(\delta),$$ (4.25)

whose divergence part precisely matches with the single cutoff computation, see eq. (4.20). In addition, also the temperature dependence of the finite part is the same in both the regularizations: their difference is finite and depends only on γ, as in eq. (4.21).

5 Volume for the time-dependent Janus BTZ geometry

In this section we will focus on the growth rate of complexity for the Janus BTZ geometry obtained through a time-dependent deformation of the BTZ black hole [49, 65]. This gravity solution corresponds to a domain wall configuration for the dilaton field along the radial direction of AdS, which connects the left and right sides of the Penrose diagram. The dilaton does not divide each boundary component into two halves, rather, it takes two different values on each boundary.

The field theory dual of this solution is not an interface CFT, but corresponds to two entangled CFTs with two different but constant values of the dilaton source, e^{ϕ_-} and e^{ϕ_+}, on each side of the Penrose diagram. The two CFTs are correlated through the bulk in a non-trivial way and the solution is time-dependent. In particular, the field theory dual starts at initial time from an out-of-equilibrium state, with an initial density for a non-conserved operator [65]. At later times, the theory thermalizes and approaches equilibrium. The initial thermofield double state is determined by

$$|\psi(0,0)\rangle = \frac{1}{\sqrt{Z}} \sum_{m,n} \langle E_m^L | E_n^R \rangle \, e^{-\frac{\beta}{4}(E_m^L + E_n^R)} |E_m^L\rangle \otimes |E_n^R\rangle.$$ (5.1)

The time evolution of this state is not invariant under the boundary time shift of eq. (2.25), because the left and the right Hamiltonians are different.

The analysis is organized in the following way. In section 5.1 we introduce the metric of the solution. In section 5.2 we restrict to the $t = 0$ case to analyze the structure of the UV divergences of the model. Then, we move to the study of the time dependence of the volume by analysing the equations of motion and specifying the boundary conditions of the problem in section 5.3. In section 5.4 we numerically determine the extremal slices and we plot the corresponding volume as a function of time.

5.1 Preliminaries

In order to find the time-dependent background, let us start form the Janus AdS$_3$ solution in eq. (2.7)

$$ds_3^2 = L^2 f(\mu) \cos^2 \mu \, ds_{\text{AdS}_3}^2 \,, \qquad ds_{\text{AdS}_3}^2 = \frac{1}{\cos^2 \mu} \left(d\mu^2 + ds_{\text{AdS}_2}^2 \right) . \tag{5.2}$$

We can replace the AdS$_3$ part of this geometry with the BTZ BH in eq. (2.23), as this solution is locally equivalent to pure AdS$_3$ (indeed, the BTZ solution can be obtained as the quotient of AdS$_3$ by a discrete group of invariances [31]). The identification between the coordinate r in eq. (2.23) and μ is given by[2]

$$\tan \mu = \pm \cosh(r_h t) \sqrt{\left(\frac{r}{r_h} \right)^2 - 1} \,. \tag{5.3}$$

This is responsible for the time-dependence of the final configuration, because μ is function both of t and r. We can introduce the Kruskal coordinates

$$V = e^{r_h(t+r_*)} \,, \qquad U = -e^{-r_h(t-r_*)} \,, \tag{5.4}$$

with tortoise coordinate

$$r_*(r) = \frac{1}{2r_h} \log \left(\frac{r - r_h}{r + r_h} \right) . \tag{5.5}$$

which can be compactified by introducing

$$V = \tan w_1 \,, \qquad U = \tan w_2 \,, \tag{5.6}$$

and finally we go back from null coordinates to timelike and spacelike ones defining

$$\tau = w_1 + w_2 \,, \qquad \mu = w_1 - w_2 \,. \tag{5.7}$$

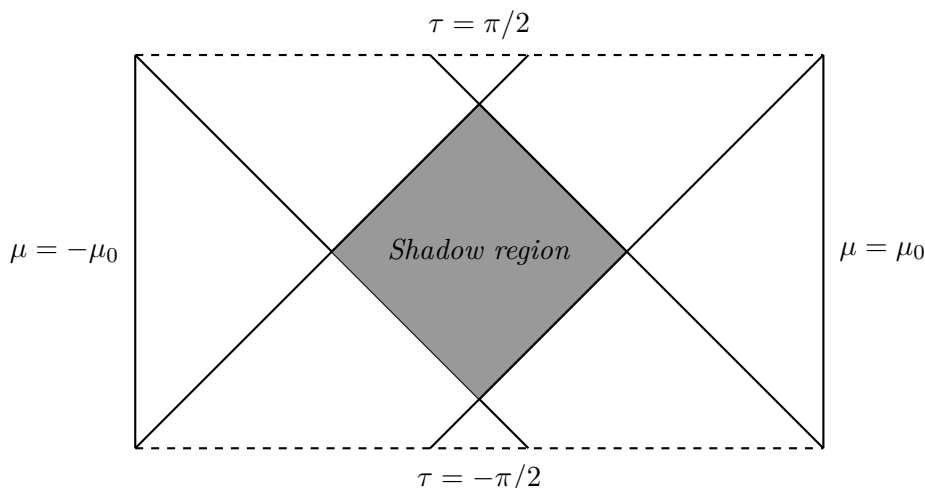Using the relation (5.3), we obtain [49, 65]

$$ds_3^2 = L^2 f(\mu) \left(-d\tau^2 + d\mu^2 + r_h^2 \cos^2 \tau d\theta^2 \right) . \tag{5.8}$$

Changing variable as in eq. (2.6), we get

$$ds_3^2 = L^2 dy^2 + L^2 f(y) \left(-d\tau^2 + r_h^2 \cos^2 \tau d\theta^2 \right) , \tag{5.9}$$

---

[2]Since the calculations in this section are mostly numerical, we use different unit conventions, in which r, r_h, t, τ, δ are dimensionless. All dimensional factors are carried out by L.

Figure 9. Penrose diagram of the Janus deformation of the BTZ black hole. The μ variable runs along horizontal lines from $-\mu_0$ to μ_0, while τ runs vertically from $-\pi/2$ to $\pi/2$. The shaded region represents the so-called *shadow region*.

with the same dilaton solution given in eq. (2.4). The Penrose diagram is shown in figure 9. Note the appearance of a "shadow region", which is causally disconnected from both the boundaries. For $\gamma = 0$ we recover the BTZ solution, which has a square Penrose diagram with no shadow region.

5.2 Volume at vanishing boundary time

The time-dependent Janus deformation of the BTZ black hole has two disconnected boundaries. In order to analyze the structure of the UV divergences of the volume, it is sufficient to consider the case where both the boundary times vanish $\tau_L = \tau_R = 0$, which implies that the extremal surface sits on a time slice at constant $\tau = 0$. This is interpreted as the complexity of formation of the Janus deformation starting from the pure BTZ background. The extremal volume reads

$$\mathcal{V}_0(\gamma) = 2L^2 \, r_h \int_0^{2\pi} d\theta \int_0^{y^*} dy \, \sqrt{f(y)}\,, \tag{5.10}$$

where introduce a UV cutoff at $y = y^*$, which we explictly determine below.

In order to compute the value of the UV cutoff consistently with the FG expansion, we notice from [66] that near the conformal boundary the metric approaches AdS space in Poincaré coordinates with radial direction ξ and time coordinate t if we make the identification

$$\xi = \frac{2}{r_h \, (1 - 2\gamma^2)^{\frac{1}{4}}} e^{-|y|} \, \cosh\left(r_h t\right)\,. \tag{5.11}$$

The compact time τ and the non-compact one t are related at the boundary by the relation

$$\tanh(r_h t) = \sin \tau\,. \tag{5.12}$$

If we set $\xi = \delta$ and $t = 0$, we get

$$y^* = -\log\left(\frac{r_h(1-2\gamma^2)^{\frac{1}{4}}}{2}\,\delta\right).\qquad(5.13)$$

The result for the volume in eq. (5.10) is

$$\mathcal{V}_0(\gamma) = 2\pi L^2\left(\frac{2}{\delta} + r_h\eta(\gamma)\right),\qquad(5.14)$$

where $\eta(\gamma)$ is defined in eq. (3.22). The difference between this volume and the volume of the standard BTZ solution (obtained for $\gamma = 0$) is

$$\Delta\mathcal{V}_0(\gamma) \equiv \mathcal{V}_0(\gamma) - \mathcal{V}_0(0) = 2\pi L^2 r_h\eta(\gamma).\qquad(5.15)$$

This quantity is indeed positive (see figure 6).

5.3 Growth rate of the volume

In this section we will address the time evolution of the ERB. In principle, the extremal surface can be specified by a function $\tau(y, \theta)$. Due to the cylindrical symmetry, the extremal τ does not depend on θ, i.e.,

$$\tau(y, \theta) = \tau(y).\qquad(5.16)$$

The volume functional can be evaluated from the metric in eq. (5.9), giving

$$\mathcal{V}(\gamma) = 4\pi L^2 r_h \int_0^{y_{\max}} dy\, f(y)\cos\left[\tau(y)\right]\sqrt{1 - f(y)\dot{\tau}^2},\qquad(5.17)$$

where the dot denotes derivative with respect to y, and $y_{\max}$ will be fixed below in terms of an appropriate UV cutoff. The Euler-Lagrange equation resulting from eq. (5.17) is

$$2\sin\tau - 3\cos\tau\, f'(y)\dot{\tau} + 2\cos\tau\, f(y)f'(y)\dot{\tau}^3 - 2f(y)\left(\sin\tau\,\dot{\tau}^2 + \cos\tau\,\ddot{\tau}\right) = 0.\qquad(5.18)$$

We then need to specify appropriate boundary conditions. We consider for simplicity the case where the boundary times satisfy

$$\tau_B \equiv \tau_L = \tau_R.\qquad(5.19)$$

In this case, the geometry is still symmetric between the left and right sides of the Penrose diagram: continuity implies that there exists a turning point for the extremal slice. For these reasons, we can impose the conditions

$$\tau(y_{\max}) = \tau(-y_{\max}) = \tau_B,\qquad \left.\frac{d\tau}{dy}\right|_{y=0} = 0.\qquad(5.20)$$

In particular, the turning point is identified by the condition

$$\tau_{\min} \equiv \tau(y = 0).\qquad(5.21)$$

Changing the boundary time τ_B, the value of $\tau_{\min}$ gets modified.

5.4 Numerical solutions and time dependence of the volume

We determine the numerical solutions to the Euler-Lagrange equations given in (5.18). This means that we find the extremal slices representing the evolution of the ERB, and we also compute numerically the integral which gives their volume.

Extremal slices. An appropriate choice of the UV cutoff is naturally determined by eq. (5.11) evaluated at $\xi = \delta$. We find

$$y_{\max}(\tau_B) = \log \left(\frac{2}{r_h\,\delta} \frac{1}{\cos\tau_B(1-2\gamma^2)^{\frac{1}{4}}} \right) . \tag{5.22}$$

This choice corresponds to the FG coordinates such that the metric on the boundary is the BTZ black hole solution, and indeed the cutoff is time-dependent as a result of the non-stationarity of the Janus deformation. Imposing the boundary conditions (5.20) at these values of the y coordinate, we get the numerical solutions in figure 10.

One may wonder which extremal volumes have a turning point that sits inside the *shadow region*. This part of the spacetime is determined by the intersection of the curves at constant value of the null coordinates

$$w_1 = \frac{1}{2}\left(\tau + \mu\right) , \qquad w_2 = \frac{1}{2}\left(\tau - \mu\right) . \tag{5.23}$$

If we impose the condition that these null lines pass through the points

$$(\mu, \tau) = \left(-\mu_0, -\frac{\pi}{2}\right) , \qquad (\mu, \tau) = \left(\mu_0, -\frac{\pi}{2}\right) , \tag{5.24}$$

then the curves that determine the shadow region for positive τ are given by

$$-\mu + \mu_0 = \tau + \frac{\pi}{2} , \qquad \mu + \mu_0 = \tau + \frac{\pi}{2} . \tag{5.25}$$

The corresponding equation in the (y, τ) coordinate system is obtained after performing the transformation

$$\tanh y = \operatorname{sn}\left(\alpha_+\mu\big|m\right) , \qquad m = \frac{\alpha_-^2}{\alpha_+^2} , \qquad \alpha_\pm^2 = \frac{1 \pm \sqrt{1-2\gamma^2}}{2} , \tag{5.26}$$

and using the definition

$$\mu_0 = \frac{1}{\alpha_+}\mathbb{K}\left(\frac{\alpha_-^2}{\alpha_+^2}\right) \geq \frac{\pi}{2} . \tag{5.27}$$

The shadow region is coloured in red in figure 10.

UV divergencies of the volume. We numerically evaluate the integral corresponding to the extremal volume (5.17), with $\tau(y)$ numerically determined by solving the differential equation (5.18) with boundary conditions (5.20). We find that the volume is a monotonically increasing function of time. A typical feature of black hole solutions like the BTZ background is that the divergences are time-independent, while the finite part brings the information about the time evolution of the system. This can be heuristically understood
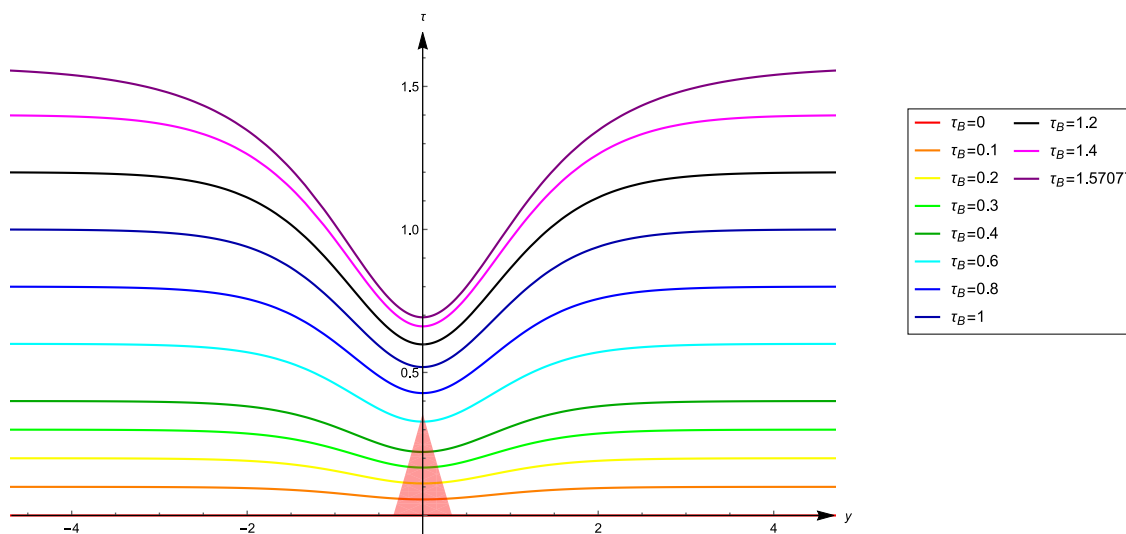
Figure 10. Plot of the numerical solutions $\tau = \tau(y)$ for different values of the boundary time τ_B. The configuration is taken to be symmetric, i.e., $\tau_L = \tau_R = \tau_B$ and the solutions have a turning point at $y = 0$, which corresponds to $\tau_{\min}$. All the extremal slices are computed by putting $\gamma = 0.5, r_h = 2.0$ and $\delta = 10^{-4}$. The solution with $\tau_B = 0$ corresponds to the case studied in section 5.2. The shadow region is shown as the red triangle in the picture.

from the fact that the time dependence is encoded in the turning point $\tau_{\min}$, and since it is determined at $y = 0$, which is far away from the boundary, it carries no UV modes. We suspect that the same phenomenon occurs for this non-stationary black hole deformation, since the choice of the UV cutoff determined from the FG expansion is such that we recover the static BTZ background at the boundary.

In order to investigate the dependence of the volume from the UV cutoff δ, we consider a fixed boundary time τ_B and we choose different values of δ scaling as

$$\delta_i = 10^{-\frac{i+2}{2}}\,, \tag{5.28}$$

with $i \in \{1, \ldots, 10\}$. If we assume that the leading divergence of the extremal volume scales as

$$\mathcal{V}_i \equiv \mathcal{V}(\delta_i, \tau_B) = \frac{4\pi}{\delta_i} + \mathcal{O}(\delta_i^0)\,, \tag{5.29}$$

see eq. (5.14), this would imply that the ratio between the volume evaluated for two consecutive values of δ_i is constant

$$\frac{\mathcal{V}_{i+1}}{\mathcal{V}_i} = \sqrt{10} \simeq 3.162\,. \tag{5.30}$$

We tested this behaviour numerically for various choices of the boundary time. We find a strong numerical evidence that the leading divergence indeed scales as δ^{-1}, see table 1.

We also notice that these ratios have a bigger error and deviate more from the analytic result as we increase the boundary time. This phenomenon can be explained by the fact that the finite term increases with time, and therefore produces a small deviation of the

Boundary time τ_B	Ratio $\mathcal{V}_{i+1}/\mathcal{V}_i$
0.2	3.159 ± 0.006
0.4	3.158 ± 0.007
0.6	3.157 ± 0.010
0.8	3.154 ± 0.014
1.0	3.151 ± 0.020
1.2	3.144 ± 0.029

Table 1. Numerical value of the ratios $\mathcal{V}_{i+1}/\mathcal{V}_i$ evaluated at various boundary times τ_B. We determined the mean value and the standard deviation from the results obtained by varying $i \in \{1, \ldots 10\}$ in the function $\delta = 10^{-\frac{i+2}{2}}$. The results must be compared with the analytic expectation $\sqrt{10} \simeq 3.162$.
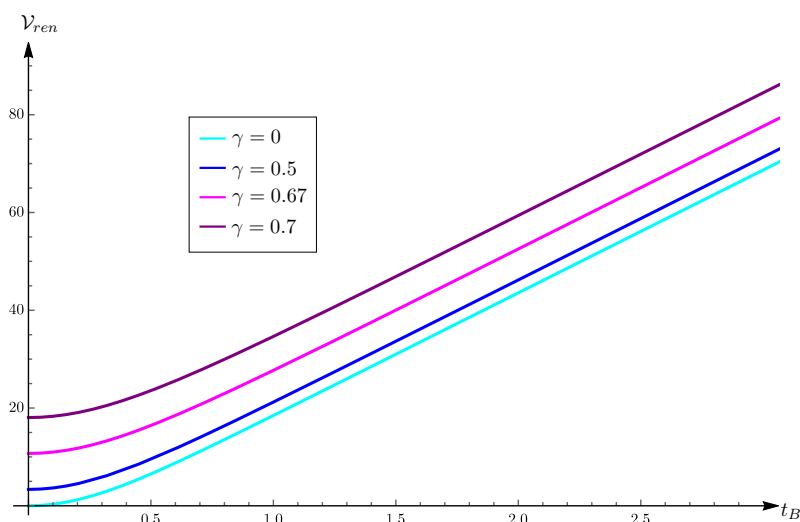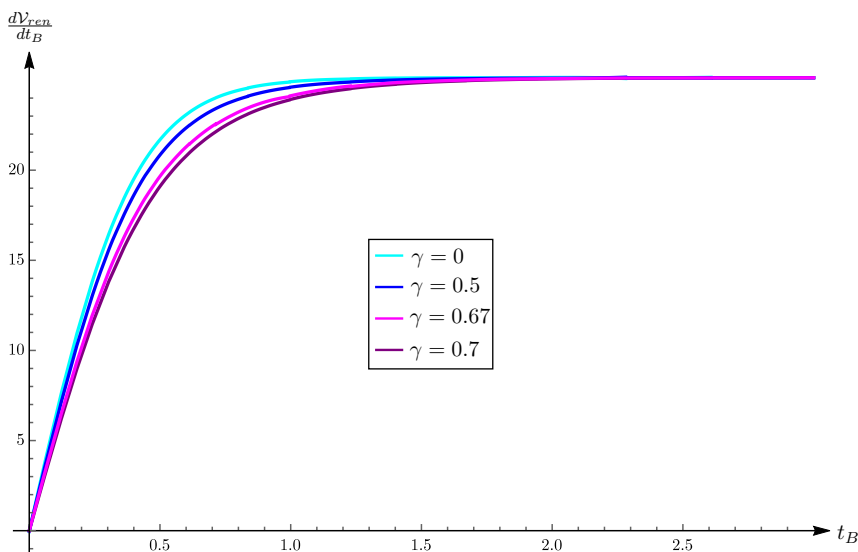

Figure 11. Time dependence of the volume of the solutions depicted in figure 10 for different values of γ, with $\delta = 10^{-4}$. The volumes $\mathcal{V}_{\mathrm{ren}}$ are renormalized after subtracting the divergence $4\pi/\delta$.

total volume from the contribution coming only from the leading divergence. One can verify that at $\tau_B = 0$ the analytic result in eq. (5.14) for the BTZ background is recovered with great accuracy.

Time dependence of the volume. In order to show the time dependence of the solution from the physical time t_B, we use the change of coordinates, valid close to the boundary, given by eq. (5.12). After subtracting the divergence $4\pi/\delta$, which is the same for all values of γ, we show in figure 11 the time dependence of the volume $\mathcal{V}_{\mathrm{ren}}$ for both the Janus deformation, plotted for different values of γ, and the pure BTZ background $\gamma = 0$. The result is a monotonically increasing function of time, which reaches a linear growth for late times. We also depict the growth-rate of the volume in figure 12. We numerically find that the rates of growth of the volume for late times are the same (within numerical uncertainties) for all the solutions with various γ.

Figure 12. Time derivative of the extemal volume of the time dependent Janus BTZ deformation for various values of γ.

According to [65], the time-dependent Janus deformation of the BTZ solution describes the thermalisation of an out-of equilibrium system, with a late-time temperature given by

$$T = \frac{r_h}{2\pi L}. \tag{5.31}$$

In addition, the area of the horizon is given by [49]

$$\mathcal{A}(\tau) = 2\pi L \, r_h \frac{\alpha_+ \sin\left(\pi/2 - \tau\right)}{\mathrm{sn}\left(\alpha_+\left(\pi/2 - \tau\right), k\right)} \xrightarrow[t_B \to \infty]{} 2\pi L \, r_h. \tag{5.32}$$

Hence, at late times

$$TS = \frac{r_h^2}{4G}, \tag{5.33}$$

which is the same value that one gets for the BTZ background. We numerically checked, for the values of γ shown in figure 13, that the asymptotic rate of the volume is

$$\frac{1}{4\pi G \, L^2} \lim_{t_B \to \infty} \frac{d\mathcal{V}_{\mathrm{ren}}}{dt_B} = TS, \tag{5.34}$$

which matches with the volume rate at late times found in [29] for the BTZ case.

We remark that the divergence of the volume is universal because it does not depend on γ. For this reason, it is meaningfull to compare the finite part of the volume with different values of the Janus deformation. We define

$$\Delta\mathcal{V}(\gamma, t_B) = \mathcal{V}(\gamma, t_B) - \mathcal{V}(0, t_B), \tag{5.35}$$

which is plotted (as a function of t_B for different γ) in figure 13. At $t_B = 0$, we have that $\Delta\mathcal{V} = \Delta\mathcal{V}_0$, given by eq. (5.15). The quantity $\Delta\mathcal{V}_0$ is positive and, in particular, for
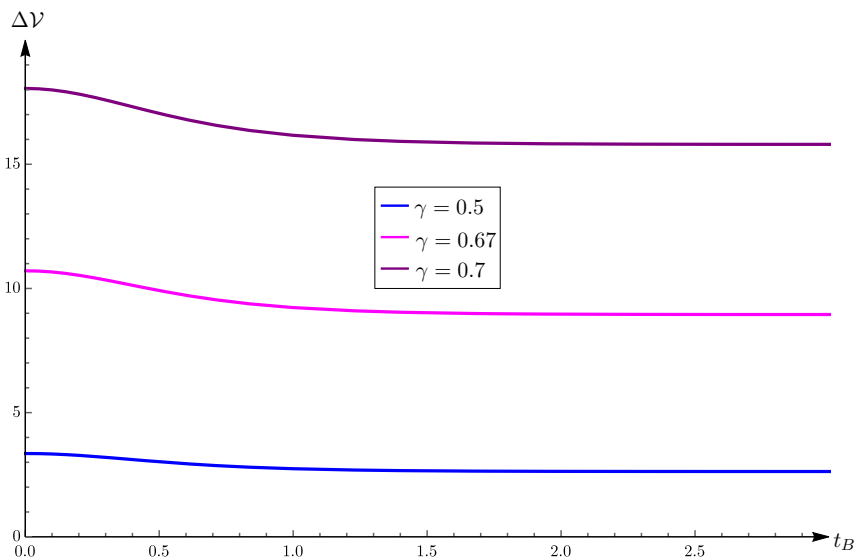
Figure 13. Plot of the quantity $\Delta\mathcal{V}(t_B)$ defined in eq. (5.35) for various values of γ. When $\gamma = 0$, this function is vanishing by construction.

$\gamma \to \sqrt{2}/2$ it diverges. Since the volume rate is a decreasing function of γ, we have that $\Delta\mathcal{V}(\gamma, t_B)$ is a decreasing function of time. The asymptotic rate does not depend on γ and so $\Delta\mathcal{V}$ approaches a constant at late times.

For $\gamma \neq 0$ the system at $t_B = 0$ starts in a out-of-equilibrium state and then thermalizes at late times. The resulting complexity rate is lower compared to the $\gamma = 0$ case: the computational power gets decreased by the time-dependent perturbation which brings the system out of equilibrium. The initial $\Delta\mathcal{V}_0$ is partially washed out at later times, but it does not approach zero asymptotically. It is surprising that the late-time volume rate is universal, in spite of the fact that different boundary values of the dilaton are dual to theories with different couplings.

5.5 Contribution of the shadow region

The consistency of holographic entanglement entropy with causality [67] imposes the requirement that the HRT surface of a given boundary region $\mathcal{A}$ lies in the causal shadow of $\mathcal{A}$. When the region $\mathcal{A}$ coincides with the left or right boundary of the Kruskal diagram, the causal shadow coincides with the shadow region in figure 9. The HRT surface of one of the boundaries of the time-dependent Janus BH lies at the center of the Penrose diagram and so it satisfies the causality bound.

Given the importance of the causal shadow for holographic entanglement entropy, it is natural to wonder about the role of the shadow region in the Complexity=Volume conjecture. The extremal volume at $t = 0$ actually crosses horizontally the entire shadow causal diamond in figure 9. It is then interesting to compute the part of the volume which is included inside the shadow region at $t = 0$. This can be achieved by restricting to the
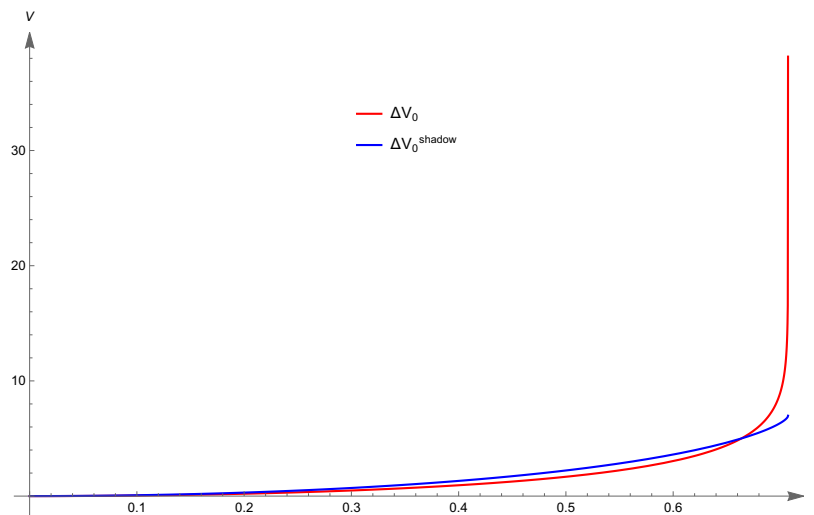
Figure 14. Volumes $\Delta\mathcal{V}_0$ and $\Delta\mathcal{V}_0^{\text{shadow}}$ as a fuction of γ. The numerical value $r_h = 1$ is chosen.

interval $\mu \in [0, \mu_0 - \frac{\pi}{2}]$ the integral in eq. (5.10). A direct evaluation gives

$$\Delta\mathcal{V}_0^{\text{shadow}}(\gamma) = 2L^2 r_h \int_0^{2\pi} d\theta \int_0^{\text{arctanh}\left[\text{sn}\left(\alpha_+\left(\mu_0 - \frac{\pi}{2}\right)|m\right)\right]} dy \sqrt{f(y)}. \tag{5.36}$$

It is interesting to compare $\Delta\mathcal{V}_0^{\text{shadow}}(\gamma)$ with $\Delta\mathcal{V}_0(\gamma)$ in eq. (5.15), see figure 14. For small γ, the dominant contribution to $\Delta\mathcal{V}_0(\gamma)$ comes indeed from the shadow region. This is not true for γ approaching to the linear dilaton regime ($\gamma \to 1/\sqrt{2}$): in this limit, the quantity $\Delta\mathcal{V}_0(\gamma)$ diverges, while the contribution arising from the shadow region is always finite, reaching the value $\pi^2 r_h/\sqrt{2}$. The linear dilaton limit lies in the strongly coupled regime from the bulk perspective, and we expect that in this limit our classical holographic calculations are not trustable.

At larger t_B, the extremal volume surface tends to escape from the shadow region. From figure 10, we can check that for $\gamma = 0.5$ and for $\tau_B > \tau_{B0} \approx 0.6$, the extremal volume starts to sit completely outside the shadow region. The escape of the extremal volume brane from the shadow region does not seem to affect the time dependence of complexity in a particularly dramatic way. As can be checked from figures 11 and 12, both the renormalised complexity and the complexity rate remain continuous and no special feature seems to appear for $\tau_B = \tau_{B0}$.

6 Conclusions

In this paper we studied subregion volume complexity for an interval of length l centered around the AdS$_3$ Janus interface. The contribution to the complexity due to the defect is log divergent in the cutoff δ, i.e.

$$\Delta\mathcal{C}(l, \gamma) = \frac{2}{3} c\,\eta(\gamma) \log\left(\frac{l}{\delta}\right) + \text{finite terms}, \tag{6.1}$$

– 34 –

where $\eta(\gamma)$ is defined in terms of elliptic integrals, see eq. (3.22) and figure 6. We performed the calculation with three different regularizations: Fefferman-Graham, single and double cutoff. The three methods give the same result for the log divergent term in eq. (6.1), while the finite terms depend on the choice of regulator. We compared the result with the AdS$_3$ Randall-Sundrum and the BCFT models, see section 3.6 for details. In all these models the leading divergence in $\Delta\mathcal{C}$ is logarithmic. This divergence is not related in an universal way to the boundary entropy ΔS, even if the two quantities share a similar qualitative behaviour.

In absence of the interface, the subregion volume complexity for the BTZ background is topologically protected by the Gauss-Bonnet theorem [32] and, therefore, does not depend on temperature. This is no longer true in the presence of the Janus interface. We computed the difference $\Delta\mathcal{C}_T$ between the finite and the zero temperature subregion complexity using both single and double cutoff regularizations. This is a finite quantity, whose temperature dependence does not depend on the regularization, i.e.

$$\Delta\mathcal{C}_T(T, l, \gamma) = \frac{2}{3} c\, \eta(\gamma)\, \log\left[\frac{2}{\pi l T} \tanh\left(\frac{\pi l T}{2}\right)\right] + \dots, \tag{6.2}$$

where the $\dots$ correspond to finite terms which are function just of γ, which parameterizes the excursion of the dilaton between the two sides of the interface. This is a decreasing function of temperature, see figure 8. It would be interesting to compute this quantity also in the RS and in the BCFT models, in order to see if there is some universality property.

As the $l \to \infty$ limit covers the whole space, we can define the total complexity by the $l \to \infty$ limit of the subregion complexity. The complexity of formation for the defect is then defined as the difference between the total complexity and its value at $\gamma = 0$. At zero temperature, the result is given by eq. (6.1), where l plays the role of an infrared regulator. At finite temperature, such expression generalizes to

$$\mathcal{C}_{\text{Defect}}^F = \frac{4}{3} c\, \eta(\gamma)\, \log\left(\frac{1}{T\,\delta}\right) + \text{finite terms}, \tag{6.3}$$

which is still logarithmically divergent. However, in this case there is no need of an infrared regulator. At finite temperature, it is also meaningful to consider the thermal complexity of formation of the Janus BTZ black hole in a geometry which already contains a defect. In this case we compute the difference between the total complexity and its value at temperature $T = 0$, to obtain

$$\mathcal{C}_{\text{Thermal}}^F = \frac{4}{3} c\, \eta(\gamma)\, \log\left(\frac{2}{\pi l T}\right). \tag{6.4}$$

Compared to eq. (6.3), this quantity is UV finite, but it requires an IR regulator l.

We also numerically computed the time evolution of the volume complexity for the time-dependent Janus BTZ black hole. In this case the boundary theory is not an interface CFT, but corresponds to two entangled CFTs with different values of the dilaton field on each of the boundaries. At $t_B = 0$, the boundary theories start from an out-of-equilibrium state and the time-dependent Janus black hole background is the gravity dual of the thermalisation process. The rate of growth of the volume as a function of the boundary time t_B is shown in figure 12.

At late time, the growth rate of the volume saturates at the same constant (proportional to TS) for all the values of γ. So the coupling does not influence the computational power of the CFT at equilibrium. This could come as a surprise given that γ determines the boundary values of the dilaton, which are dual to the couplings of the boundary CFTs. We find that at early times, where the dual field theory is in an out-of-equilibrium state for $\gamma \neq 0$, the Janus deformation always decreases the complexity growth rate compared to the BTZ case. Being out of equilibrium decreases the computational power of the CFT.

In this paper we investigated several aspects of the CV conjecture in AdS$_3$ Janus geometries. Several open questions call for further investigation:

- It would be interesting to extend our analysis of the complexity of the time-dependent Janus BTZ BH to more general geometries. For regions made by the union of two segments on different sides of the Kruskal diagram, there is a phase transition in the topology of the HRT surface: depending on the size of the segments, the HRT surface can be connected or disconnected [66]. This should be reflected in a discontinuity of subregion complexity as a function of the length of the segment; similar discontinuities in subregion complexity appear also for regions made by two segments in AdS$_3$ Poincaré patch, see e.g. [32, 33].

- Another direction is the generalization to higher dimensions, for example to Janus AdS$_5$. This is the topic of a follow-up work [68]. In this case the leading order divergence is power-like, and depends on the regularization method that is used. Subleading logarithmic divergences instead turn out to be independent of the regularization method. This result points towards a universal property typical of the coefficient of the logarithmic divergences, as we also observed in the three-dimensional case considered here.

- An important topic for further investigation is the complexity=action conjecture [27]. For AdS$_3$ Randall-Sundrum [51] and BCFT [52, 53] the action complexity due to the defect is finite, and so it provides a situation where the CV and the CA conjecture give radically different outcomes. In higher dimension BCFT, it turns out that CV and CA have instead the same leading-order divergence structure [52]. It would be interesting to investigate the case of the Janus interface, both in AdS$_3$ and in AdS$_5$, to check if this behaviour is universal for defects.

- It would be interesting to compare the holographic result with a direct calculation of complexity on the field theory side. In [53] circuit complexity was computed in a free field theory with boundary, following the approach introduced in [18]. Even if the free field theory calculation and the holographic dual are not directly related, it is interesting that the result is logarithmically divergent, as in the CV case. The absence of logarithmic divergences in CA so seems to disfavour this proposal. It would be interesting to perform the calculation of the complexity of the defect also in conformal field theory, following the approach in [21–23]. The CFT calculation should be more directly related to the holographic dual and may give further insights on the problem of identifying the correct holographic dual of quantum computational complexity.

Acknowledgments

We thank G. Bruno De Luca for valuable discussions. The authors S.B. acknowledge support from the Independent Research Fund Denmark grant number DFF-6108-00340 "Towards a deeper understanding of black holes with non-relativistic holography" and from DFF-FNU through grant number DFF-4002-00037.

A Jacobi elliptic functions and elliptic integrals

We work with the standard Jacobi elliptic functions and elliptic integrals defined along the lines of [69]. We use the incomplete elliptic integrals

$$\mathbb{F}\left(x \,|\, m\right) = \int_0^x \frac{d\theta}{\sqrt{1 - m\sin^2\theta}} \,, \tag{A.1}$$

$$\mathbb{E}\left(x \,|\, m\right) = \int_0^x d\theta \sqrt{1 - m\sin^2\theta} \,, \tag{A.2}$$

$$\Pi\left(n; x \,|\, m\right) = \int_0^x \frac{d\theta}{\left(1 - n\sin^2\theta\right)\sqrt{1 - m\sin^2\theta}}. \tag{A.3}$$

of the first, second and third kind, respectively. The complete elliptic integrals are defined as

$$\mathbb{F}\left(\frac{\pi}{2}\bigg|\, m\right) = \mathbb{K}(m) \,, \quad \mathbb{E}\left(\frac{\pi}{2}\bigg|\, m\right) = \mathbb{E}(m) \,, \quad \Pi\left(n; \frac{\pi}{2}\bigg|\, m\right) = \Pi\left(n \,|\, m\right) \,. \tag{A.4}$$

We also use the Jacobi amplitude $\varphi = \mathrm{am}(x|m)$ which is the inverse of $\mathbb{F}\left(x \,|\, m\right)$

$$x = \mathbb{F}\left(\mathrm{am}(x|m) \,|\, m\right) \,. \tag{A.5}$$

The Jacobi elliptic functions are defined as

$$\mathrm{sn}\left(x \,|\, m\right) = \sin\varphi, \quad \mathrm{cn}\left(x \,|\, m\right) = \cos\varphi \quad \text{and} \quad \mathrm{dn}\left(x \,|\, m\right) = \sqrt{1 - m\sin^2\varphi}, \tag{A.6}$$

such that $\mathrm{sn}\left(\mathbb{K}(m) \,|\, m\right) = 1$ and $\mathrm{cn}\left(\mathbb{K}(m) \,|\, m\right) = 0$.

Open Access. This article is distributed under the terms of the Creative Commons Attribution License ([CC-BY 4.0](https://creativecommons.org/licenses/by/4.0/)), which permits any use, distribution and reproduction in any medium, provided the original author(s) and source are credited.

References

[1] S. Ryu and T. Takayanagi, *Holographic derivation of entanglement entropy from AdS/CFT*, *Phys. Rev. Lett.* **96** (2006) 181602 [`hep-th/0603001`] [INSPIRE].

[2] V.E. Hubeny, M. Rangamani and T. Takayanagi, *A covariant holographic entanglement entropy proposal*, *JHEP* **07** (2007) 062 [`arXiv:0705.0016`] [INSPIRE].

[3] A. Lewkowycz and J. Maldacena, *Generalized gravitational entropy*, *JHEP* **08** (2013) 090 [`arXiv:1304.4926`] [INSPIRE].

[4] T. Faulkner, A. Lewkowycz and J. Maldacena, *Quantum corrections to holographic entanglement entropy*, *JHEP* **11** (2013) 074 [`arXiv:1307.2892`] [INSPIRE].

[5] A. Almheiri, N. Engelhardt, D. Marolf and H. Maxfield, *The entropy of bulk quantum fields and the entanglement wedge of an evaporating black hole*, *JHEP* **12** (2019) 063 [arXiv:1905.08762] [INSPIRE].

[6] G. Penington, *Entanglement wedge reconstruction and the information paradox*, *JHEP* **09** (2020) 002 [arXiv:1905.08255] [INSPIRE].

[7] A. Almheiri, R. Mahajan, J. Maldacena and Y. Zhao, *The Page curve of Hawking radiation from semiclassical geometry*, *JHEP* **03** (2020) 149 [arXiv:1908.10996] [INSPIRE].

[8] L. Susskind, *Computational complexity and black hole horizons*, *Fortsch. Phys.* **64** (2016) 24 [*Addendum ibid.* **64** (2016) 44] [arXiv:1403.5695] [INSPIRE].

[9] M. Miyaji, T. Numasawa, N. Shiba, T. Takayanagi and K. Watanabe, *Distance between quantum states and gauge-gravity duality*, *Phys. Rev. Lett.* **115** (2015) 261602 [arXiv:1507.07555] [INSPIRE].

[10] M. Alishahiha, *Holographic complexity*, *Phys. Rev. D* **92** (2015) 126009 [arXiv:1509.06614] [INSPIRE].

[11] D. Stanford and L. Susskind, *Complexity and shock wave geometries*, *Phys. Rev. D* **90** (2014) 126007 [arXiv:1406.2678] [INSPIRE].

[12] L. Susskind, *Entanglement is not enough*, *Fortsch. Phys.* **64** (2016) 49 [arXiv:1411.0690] [INSPIRE].

[13] M.A. Nielsen, *A geometric approach to quantum circuit lower bounds*, *Quant. Informat. Comput.* **6** (2006) 213 [quant-ph/0502070].

[14] M.R. Dowling and M.A. Nielsen, *The geometry of quantum computation*, *Quant. Informat. Comput.* **8** (2010) 861 [quant-ph/0701004].

[15] A.R. Brown, L. Susskind and Y. Zhao, *Quantum complexity and negative curvature*, *Phys. Rev. D* **95** (2017) 045010 [arXiv:1608.02612] [INSPIRE].

[16] A.R. Brown and L. Susskind, *Complexity geometry of a single qubit*, *Phys. Rev. D* **100** (2019) 046020 [arXiv:1903.12621] [INSPIRE].

[17] R. Auzzi, S. Baiguera, G.B. De Luca, A. Legramandi, G. Nardelli and N. Zenoni, *Geometry of quantum complexity*, *Phys. Rev. D* **103** (2021) 106021 [arXiv:2011.07601] [INSPIRE].

[18] R. Jefferson and R.C. Myers, *Circuit complexity in quantum field theory*, *JHEP* **10** (2017) 107 [arXiv:1707.08570] [INSPIRE].

[19] S. Chapman, M.P. Heller, H. Marrochio and F. Pastawski, *Toward a definition of complexity for quantum field theory states*, *Phys. Rev. Lett.* **120** (2018) 121602 [arXiv:1707.08582] [INSPIRE].

[20] R. Khan, C. Krishnan and S. Sharma, *Circuit complexity in fermionic field theory*, *Phys. Rev. D* **98** (2018) 126001 [arXiv:1801.07620] [INSPIRE].

[21] P. Caputa and J.M. Magan, *Quantum computation as gravity*, *Phys. Rev. Lett.* **122** (2019) 231302 [arXiv:1807.04422] [INSPIRE].

[22] J. Erdmenger, M. Gerbershagen and A.-L. Weigel, *Complexity measures from geometric actions on Virasoro and Kac-Moody orbits*, *JHEP* **11** (2020) 003 [arXiv:2004.03619] [INSPIRE].

[23] N. Chagnet, S. Chapman, J. de Boer and C. Zukowski, *Complexity for conformal field theories in general dimensions*, arXiv:2103.06920 [INSPIRE].

[24] P. Caputa, N. Kundu, M. Miyaji, T. Takayanagi and K. Watanabe, *Liouville action as path-integral complexity: from continuous tensor networks to AdS/CFT*, *JHEP* **11** (2017) 097 [arXiv:1706.07056] [INSPIRE].

[25] D.E. Parker, X. Cao, A. Avdoshkin, T. Scaffidi and E. Altman, *A universal operator growth hypothesis*, *Phys. Rev. X* **9** (2019) 041017 [arXiv:1812.08657] [INSPIRE].

[26] J.L.F. Barbón, E. Rabinovici, R. Shir and R. Sinha, *On the evolution of operator complexity beyond scrambling*, *JHEP* **10** (2019) 264 [arXiv:1907.05393] [INSPIRE].

[27] A.R. Brown, D.A. Roberts, L. Susskind, B. Swingle and Y. Zhao, *Holographic complexity equals bulk action?*, *Phys. Rev. Lett.* **116** (2016) 191301 [arXiv:1509.07876] [INSPIRE].

[28] A.R. Brown, D.A. Roberts, L. Susskind, B. Swingle and Y. Zhao, *Complexity, action, and black holes*, *Phys. Rev. D* **93** (2016) 086006 [arXiv:1512.04993] [INSPIRE].

[29] D. Carmi, S. Chapman, H. Marrochio, R.C. Myers and S. Sugishita, *On the time dependence of holographic complexity*, *JHEP* **11** (2017) 188 [arXiv:1709.10184] [INSPIRE].

[30] D. Carmi, R.C. Myers and P. Rath, *Comments on holographic complexity*, *JHEP* **03** (2017) 118 [arXiv:1612.00433] [INSPIRE].

[31] M. Bañados, M. Henneaux, C. Teitelboim and J. Zanelli, *Geometry of the $(2+1)$ black hole*, *Phys. Rev. D* **48** (1993) 1506 [*Erratum ibid.* **88** (2013) 069902] [gr-qc/9302012] [INSPIRE].

[32] R. Abt et al., *Topological complexity in AdS_3/CFT_2*, *Fortsch. Phys.* **66** (2018) 1800034 [arXiv:1710.01327] [INSPIRE].

[33] R. Auzzi, S. Baiguera, A. Legramandi, G. Nardelli, P. Roy and N. Zenoni, *On subregion action complexity in AdS_3 and in the BTZ black hole*, *JHEP* **01** (2020) 066 [arXiv:1910.00526] [INSPIRE].

[34] R. Abt, J. Erdmenger, M. Gerbershagen, C.M. Melby-Thompson and C. Northe, *Holographic subregion complexity from kinematic space*, *JHEP* **01** (2019) 012 [arXiv:1805.10298] [INSPIRE].

[35] C.A. Agón, M. Headrick and B. Swingle, *Subsystem complexity and holography*, *JHEP* **02** (2019) 145 [arXiv:1804.01561] [INSPIRE].

[36] R. Auzzi, S. Baiguera, A. Mitra, G. Nardelli and N. Zenoni, *Subsystem complexity in warped AdS*, *JHEP* **09** (2019) 114 [arXiv:1906.09345] [INSPIRE].

[37] B. Chen, W.-M. Li, R.-Q. Yang, C.-Y. Zhang and S.-J. Zhang, *Holographic subregion complexity under a thermal quench*, *JHEP* **07** (2018) 034 [arXiv:1803.06680] [INSPIRE].

[38] R. Auzzi, G. Nardelli, F.I. Schaposnik Massolo, G. Tallarita and N. Zenoni, *On volume subregion complexity in Vaidya spacetime*, *JHEP* **11** (2019) 098 [arXiv:1908.10832] [INSPIRE].

[39] E. Caceres, S. Chapman, J.D. Couch, J.P. Hernández, R.C. Myers and S.-M. Ruan, *Complexity of mixed states in QFT and holography*, *JHEP* **03** (2020) 012 [arXiv:1909.10557] [INSPIRE].

[40] P. Calabrese and J.L. Cardy, *Entanglement entropy and quantum field theory*, *J. Stat. Mech.* **0406** (2004) P06002 [hep-th/0405152] [INSPIRE].

[41] I. Affleck and A.W.W. Ludwig, *Universal noninteger 'ground state degeneracy' in critical quantum systems*, *Phys. Rev. Lett.* **67** (1991) 161 [INSPIRE].

[42] L. Randall and R. Sundrum, *An alternative to compactification*, *Phys. Rev. Lett.* **83** (1999) 4690 [hep-th/9906064] [INSPIRE].

[43] T. Azeyanagi, A. Karch, T. Takayanagi and E.G. Thompson, *Holographic calculation of boundary entropy*, *JHEP* **03** (2008) 054 [arXiv:0712.1850] [INSPIRE].

[44] A. Bhattacharya, A. Bhattacharyya, P. Nandy and A.K. Patra, *Islands and complexity of eternal black hole and radiation subsystems for a doubly holographic model*, *JHEP* **05** (2021) 135 [arXiv:2103.15852] [INSPIRE].

[45] T. Takayanagi, *Holographic dual of BCFT*, *Phys. Rev. Lett.* **107** (2011) 101602 [arXiv:1105.5165] [INSPIRE].

[46] M. Fujita, T. Takayanagi and E. Tonni, *Aspects of AdS/BCFT*, *JHEP* **11** (2011) 043 [arXiv:1108.5152] [INSPIRE].

[47] M. Flory, *A complexity/fidelity susceptibility g-theorem for $AdS_3/BCFT_2$*, *JHEP* **06** (2017) 131 [arXiv:1702.06386] [INSPIRE].

[48] D. Bak, M. Gutperle and S. Hirano, *A dilatonic deformation of AdS_5 and its field theory dual*, *JHEP* **05** (2003) 072 [hep-th/0304129] [INSPIRE].

[49] D. Bak, M. Gutperle and S. Hirano, *Three dimensional Janus and time-dependent black holes*, *JHEP* **02** (2007) 068 [hep-th/0701108] [INSPIRE].

[50] Y. Nakata, T. Takayanagi, Y. Taki, K. Tamaoka and Z. Wei, *New holographic generalization of entanglement entropy*, *Phys. Rev. D* **103** (2021) 026005 [arXiv:2005.13801] [INSPIRE].

[51] S. Chapman, D. Ge and G. Policastro, *Holographic complexity for defects distinguishes action from volume*, *JHEP* **05** (2019) 049 [arXiv:1811.12549] [INSPIRE].

[52] Y. Sato and K. Watanabe, *Does boundary distinguish complexities?*, *JHEP* **11** (2019) 132 [arXiv:1908.11094] [INSPIRE].

[53] P. Braccia, A.L. Cotrone and E. Tonni, *Complexity in the presence of a boundary*, *JHEP* **02** (2020) 051 [arXiv:1910.03489] [INSPIRE].

[54] D. Bak, *Information metric and Euclidean Janus correspondence*, *Phys. Lett. B* **756** (2016) 200 [arXiv:1512.04735] [INSPIRE].

[55] N.S. Mazhari, D. Momeni, S. Bahamonde, M. Faizal and R. Myrzakulov, *Holographic complexity and fidelity susceptibility as holographic information dual to different volumes in AdS*, *Phys. Lett. B* **766** (2017) 94 [arXiv:1609.00250] [INSPIRE].

[56] D.Z. Freedman, C. Núñez, M. Schnabl and K. Skenderis, *Fake supergravity and domain wall stability*, *Phys. Rev. D* **69** (2004) 104027 [hep-th/0312055] [INSPIRE].

[57] I. Papadimitriou and K. Skenderis, *Correlation functions in holographic RG flows*, *JHEP* **10** (2004) 075 [hep-th/0407071] [INSPIRE].

[58] M. Chiodaroli, M. Gutperle and L.-Y. Hung, *Boundary entropy of supersymmetric Janus solutions*, *JHEP* **09** (2010) 082 [arXiv:1005.4433] [INSPIRE].

[59] D. Bak, M. Gutperle and R.A. Janik, *Janus black holes*, *JHEP* **10** (2011) 056 [arXiv:1109.2736] [INSPIRE].

[60] D. Bak, C. Kim, S.-H. Yi and J. Yoon, *Unitarity of entanglement and islands in two-sided Janus black holes*, *JHEP* **01** (2021) 155 [arXiv:2006.11717] [INSPIRE].

[61] J. Estes, K. Jensen, A. O'Bannon, E. Tsatis and T. Wrase, *On holographic defect entropy*, *JHEP* **05** (2014) 084 [`arXiv:1403.6475`] [ɪɴSPIRE].

[62] D. Bak, A. Gustavsson and S.-J. Rey, *Conformal Janus on Euclidean sphere*, *JHEP* **12** (2016) 025 [`arXiv:1605.00857`] [ɪɴSPIRE].

[63] M. Gutperle and A. Trivella, *Note on entanglement entropy and regularization in holographic interface theories*, *Phys. Rev. D* **95** (2017) 066009 [`arXiv:1611.07595`] [ɪɴSPIRE].

[64] S. Chapman, H. Marrochio and R.C. Myers, *Complexity of formation in holography*, *JHEP* **01** (2017) 062 [`arXiv:1610.08063`] [ɪɴSPIRE].

[65] D. Bak, M. Gutperle and A. Karch, *Time dependent black holes and thermal equilibration*, *JHEP* **12** (2007) 034 [`arXiv:0708.3691`] [ɪɴSPIRE].

[66] Y. Nakaguchi, N. Ogawa and T. Ugajin, *Holographic entanglement and causal shadow in time-dependent Janus black hole*, *JHEP* **07** (2015) 080 [`arXiv:1412.8600`] [ɪɴSPIRE].

[67] M. Headrick, V.E. Hubeny, A. Lawrence and M. Rangamani, *Causality* & *holographic entanglement entropy*, *JHEP* **12** (2014) 162 [`arXiv:1408.6300`] [ɪɴSPIRE].

[68] S. Baiguera, S. Bonansea and K. Toccacelo, *Volume complexity for the non-supersymmetric Janus AdS₅ geometry*, [`arXiv:2105.12743`] [ɪɴSPIRE].

[69] M. Abramowitz and I. Stegun, *Handbook of mathematical functions*, fifth edition, Dover, New York, NY, U.S.A. (1964).